

AD-A209 152



GLIDER GROUND EFFECT INVESTIGATION

THESIS

Nathan H. Jones

Captain, USAF

AFIT/GAE/ENY/89J-2

Best Available Copy

DEPARTMENT OF THE AIR FORCE

AIR UNIVERSITY

AIR FORCE INSTITUTE OF TECHNOLOGY

Wright-Patterson Air Force Base, Ohio

This document has been approved
for public release and sales in
distribution is unlimited.

89 6 19 073

DTIC
ELECTE
JUN 20 1989
S & E D

AFIT/GAE/ENY/89

GLIDER GROUND EFFECT INVESTIGATION

THESIS

Nathan H. Jones
Captain, USAF

AFIT/GAE/ENY/89J-2

Approved for public release; distribution unlimited

GLIDER GROUND EFFECT INVESTIGATION

THESIS

Presented to the Faculty of the School of Engineering
of the Air Force Institute of Technology

Air University

In Partial Fulfillment of the
Requirements for the Degree of
Master of Science in Aeronautical Engineering

Nathan H. Jones, B.S.
Captain, USAF

May 1989



Accession For	
NTIS GRA&I	<input checked="checked" type="checkbox"/>
DTIC TAB	<input type="checkbox"/>
Unannounced	<input type="checkbox"/>
Justification	
By _____	
Distribution/	
Availability Codes	
Avail and/or	
Dist	Special
A-1	

Approved for public release; distribution unlimited

Preface

One day in the fall of 1986, I was enjoying myself on a particularly good soaring flight. I had just gained 3000 feet of altitude in a thermal and had only drifted 5 miles from my airfield. I slowly turned the glider back toward the airfield and set up a constant airspeed glide to get the magic maximum lift to drag ratio. A casual glance below alarmed me; however. I had no groundspeed; the wind was keeping me over the same spot of ground! I now knew that I must fly faster than the maximum lift to drag airspeed, but how much faster? Too fast and I would lose all my altitude, too slow and the wind would keep me from making sufficient groundspeed. I next thought about using ground effect to squeeze out the last few thousand feet to the airport. The winds would be less at low altitude and my induced drag would be reduced, allowing me to "float" farther. I delayed the ground effect decision until the last minute.

This decision confronts glider pilots around the world every day. Some experienced glider pilots adamantly claim that ground effect can greatly extend glide range, and they claim to have floated several thousand feet in ground effect. Indeed, ground effect theory predicts a large reduction in induced drag, and one should be able to glide farther with this reduced drag. This thesis investigates the possibility of extending glide range using ground effect, and it also gives the only glider flight test

evaluation of ground effect theory. It answers the question of whether to use ground effect for all glider pilots.

I was fortunate to have some excellent help with this thesis. This thesis is an extension of the United States Air Force (USAF) Test Pilot School (TPS) Class 1988A Have Effect flight test project. I want to thank the other 4 members of the Have Effect test team for their hard work and ingenuity in getting this test done. These team members were: Capt Chris Hadfield, Royal Canadian Air Force, and Maj Chuck Louie, Capt Rick Husband, and Capt Ken Green, USAF. I also want to thank my thesis advisor Maj Dan Gleason for the encouragement he has given me and the help in coordinating this thesis with the Air Force Institute of Technology (AFIT) and TPS. I also need to acknowledge the USAF Test Pilot School, which provided two gliders and all of the test equipment. The final acknowledgement is to the Air Force Flight Test Center (AFFTC) for providing the finest flight test facility in the world for this project, Rogers dry lakebed and its radar tracking facilities.

In case you were wondering, I decided not to use ground effect on my glider flight. I entered a short final approach with about 200 feet of altitude, just enough to make a normal landing with. As this thesis shows, it was a good thing I didn't try to use ground effect after all.

Nathan H. Jones

Table of Contents

	Page
Preface	ii
List of Figures	vi
List of Tables	vii
Notation	viii
Abstract	xi
I. Introduction	1
Background	1
Objectives	2
Approach	3
Test Articles and Instrumentation	6
II. Aerodynamic Theory	9
Aerodynamics of Drag	9
Estimation of Drag Characteristics	13
Ground Effect Theory	19
Atmospheric Wind Model	24
III. Simulation	28
Equations of Motion	28
Glider Simulation	32
IV. Optimization Theory	38
Secant Algorithm	38
Steepest Gradient Algorithm	40
Quadratic Spline Interpolation	42
Newton's Method for Nonlinear Systems	46
Gauss-Newton Algorithm	50
V. Flight Test	54
Overview	54
Test Conditions	54
Initial Tests	55
Drag Polar In Ground Effect	56
Flight Profile Familiarization	66
Flight Profile Development	71
Flight Profile Verification	78

VI.	Flight Profile Optimization	83
	Methods	83
	Results	89
	Practical Applications	101
VII.	Conclusions and Recommendations	103
	Conclusions	103
	Recommendations	108
	Appendix A: Glider Descriptions	110
	Bibliography	115
	Vita	116

List of Figures

	Page
1.1 Speed Course Set Up	8
2.1 Lifting Line Theory of Ground Effect	21
2.2 Predicted Reduction in Grob Induced Drag Due to Ground Effect	23
2.3 Predicted Reduction in Grob Total Drag Due to Ground Effect	25
2.4 Wind Profile Model	26
3.1 Glider in Near Steady Flight	31
4.1 Quadratic Spline Interpolation	43
4.2 Points Used in Jacobian and Gradient Approximations	49
5.1 Grob Drag Polar Out of Ground Effect	57
5.2 Ground Effect Drag Reduction	63
5.3 Revised Ground Effect Drag Reduction Prediction	65
5.4 Standard and Test Flight Profiles	66
5.5 Glide Range Versus Level Deceleration Altitude	75
5.6 Glide Range Versus Pushover Altitude	77
6.1 Grob Performance Polar	85
6.2 Range Gain Versus Density Altitude	93
6.3 Range Gain Versus Altitude to Wingspan Ratio .	95
6.4 Range Gain Versus Level Deceleration Altitude .	96
6.5 Range Gain Versus Error in Penetration Airspeed	97
6.6 Range Gain Versus Variation in Parasite Drag Coefficient	98
6.7 Range Gain Versus Wing Loading Variation . . .	99
6.8 Range Gain Versus Variation in Induced Drag Factor	100
A.1 Grob G-103 Twin II	111
A.2 Let L-13 Blanik	113

List of Tables

	Page
2.1 Glider Characteristics	14
2.2 Estimate of Glider Parasite Drag Coefficients	15
2.3 Estimate of Glider Induced Drag Factors . . .	19
5.1 Ground Effect Drag Parameters	61
5.2 Flight Profile Development Test Matrix	74
5.3 Profile Development Test Results	76
5.4 Test Aircraft Comparison	79
5.5 Profile Verification Test Matrix	80
5.6 Profile Verification Test Results	81
6.1 Grob Optimum Profiles	89
6.2 Blanik Flaps Up Optimum Profiles	90
6.3 Blanik Flaps Down Optimum Profiles	91

Notation

AFB	Air Force Base
AFFTC	Air Force Flight Test Center
AFIT	Air Force Institute of Technology
AGL	Above Ground Level
a_n	Normal Acceleration
AR	Wing Aspect Ratio, b^2/S
a_t	Tangential Acceleration
Avg	Average
b	Wingspan
Blanik	Let L-13 Blanik Glider
\bar{c}	Mean Aerodynamic Chord
CA	California
C_D	Drag Coefficient
C_{Di}	Induced Drag Coefficient
C_{Do}	Parasite Drag Coefficient
C_f	Turbulent Flat Plate Friction Coefficient
C_L	Lift Coefficient
d	Fuselage Equivalent Diameter, $\left(\frac{S_{fuse}}{0.7875}\right)^{0.5}$
decel	Deceleration
e	Oswald's Efficiency Factor
e'	Wing Efficiency Factor (8:11-9)
F	Ground Effect Induced Drag Reduction Factor
ft	Feet
g	Gravitational Acceleration

G	Gravitational Acceleration Unit
Grob	Grob G-103 Twin II Glider
h	Height Above Ground Level
h_{decel}	Level Deceleration Height Above Ground Level
h_{pull}	Pullup Starting Height Above Ground Level
h_{push}	Pushover Starting Height Above Ground Level
J	Jacobian Matrix of Second Partial Derivatives
k	Induced Drag Factor
k_0	Induced Drag Factor Out of Ground Effect
KCAS	Knots Calibrated Airspeed
KTAS	Knots True Airspeed
L	Aircraft Lift
L	Airfoil Maximum Thickness Parameter (8:11-13)
l_B	Fuselage length
m	Aircraft Mass
Max	Maximum
Min	Minimum
n	Aircraft Load Factor
NASA	National Aeronautics and Space Administration
NO.	Number
n_{pull}	Pullout Load Factor
n_{push}	Pushover Load Factor
R	Lifting Surface Correlation Factor (8:11-13)
S	Wing Planform Area
S_e	Wing Exposed Surface Area
S_{fuse}	Fuselage Wetted Area

S_{horiz}	Horizontal Tail Planform Area
Std	Standard
S_{vert}	Vertical Tail Planform Area
t	Time
t/c	Airfoil Maximum Thickness to Chord Ratio
TG	Test Group
V	True Airspeed
V_u	Wind Velocity at 900 Feet Above Ground Level
V_w	Wind Velocity
V_M	Manuever Airspeed
V_{NE}	Never Exceed Airspeed
W	Aircraft Weight
W/S	Wing Loading
X_{ref}	Reference Ground Distance

Greek

α	Angle of Attack
∇	Gradient Vector
∂	Partial Derivative
Δ	Small Increment
γ	Flight Path Angle
γ_{glider}	Flight Path Angle Relative to Surrounding Atmosphere
γ_{ground}	Flight Path Angle Relative to Earth Fixed Coordinates
γ_{dive}	Dive Angle
ρ	Air Density

Abstract

This research used glider flight tests and optimized glider simulations to evaluate the aerodynamics of ground effect and to determine the optimum flight profile for maximum gliding range in gliders. A series of 122 sorties were flown in the Grob G-103 Twin II and the Let L-13 Blanik gliders on a specially designed very low altitude speed course, at the ~~Air Force Flight Test Center, Edwards AFB,~~ California from 21 September to 25 October ~~1988~~. Radar tracking data were used to determine the glider position and velocity, and a 3 degree of freedom glider performance simulation was used to determine the glider parasite and induced drag coefficients in ground effect. Lifting line derived predictions of ground effect induced drag reduction developed by Dr. Sighard Hoerner were found to be accurate at altitudes above 20 percent wingspan but were up to 16 percent too optimistic at low altitudes. A revised prediction of ground effect induced drag reduction was developed based on the flight test data, and this revised prediction was used along with a turbulent boundary layer wind model in two optimization algorithms to develop the optimum flight profiles for maximum range gliding flight.

Although flight tests of these profiles in near perfect test conditions showed that glide range gains of up to 1179 feet were possible over penetration airspeed glides, these profiles involve dangerous low altitude maneuvers and are not predicted to give significant range gains over penetration airspeed glides in winds up to 50 knots. Therefore, the results of this research are a revised prediction of ground effect at low altitude and the confirmation that penetration airspeed glides provide maximum glide range under normal circumstances.

GLIDER GROUND EFFECT INVESTIGATION

I. Introduction

Background

The aerodynamic effect of flying close to the ground has been analyzed and, to a small degree, tested in wind tunnels and flight since the 1920s. Yet according to officials of the Soaring Society of America, the results of this analysis and testing has never been applied to gliders. Ground effect causes reductions in aircraft drag and wind velocity, both of which could significantly increase a glider's maximum range. This research was conducted to evaluate previous predictions of ground effect and to determine the optimum flight profile to achieve maximum range in a glider considering ground effect.

Dr. Sighard Hoerner in his book Fluid-Dynamic Lift (Ref 6) incorporated the majority of all previous ground effect analyses and testing. His theoretical predictions of ground effect showed that the aircraft drag due to lift (induced drag) decreases exponentially as altitude above ground level (AGL) decreases. Also, since ground effect reduces only the aircraft's induced drag, the drag reduction is greatest at low airspeeds where the induced drag is greatest. Thus, ground effect is most significant when an aircraft is low to

the ground and slow (6:20-6 to 20-10).

Glider pilots are currently taught to fly a shallow constant airspeed glide which ignores ground effect in order to achieve maximum range. Under no wind conditions, the airspeed giving a maximum lift to drag ratio is flown. Maximizing the lift to drag ratio results in maximizing the ground distance covered to altitude lost ratio in calm air. When headwinds or tailwinds are present, a different airspeed giving the maximum ground distance covered to altitude lost ratio is flown. These airspeeds do indeed give the maximum range outside of ground effect, but under some conditions a longer range results from terminating the constant airspeed glide early, diving more steeply to gain airspeed, and leveling out very low above the ground. Determining when and how to transition from the constant airspeed glide to level flight in ground effect constitutes the problem of determining the optimum flight profile for maximum range. A flight profile which extends a glider's maximum range over that achievable with a constant airspeed glide could save the gliders and lives of many glider pilots who find themselves short of an intended landing field at low altitude.

Objectives

1. Develop a glider performance simulation based on ground effect theory.

2. Determine the airspeed instrument errors of the Grob G-103.
3. Determine the Grob G-103 drag polar through analysis and flight test.
4. Quantify the amount of drag reduction experienced by a Grob G-103 glider at 8 altitudes ranging from 4 to 100 feet AGL under windless conditions.
5. Compare the measured drag reduction due to ground effect to the theoretical drag reduction.
6. Develop and flight test standard and test flight profiles to determine Grob glide range variations in calm air.
7. Flight test standard and test profiles for maximum range in a Let L-13 Blanik glider.
8. Develop the optimum profile to fly for maximum range with and without wind.

Approach

In order to accomplish this project's 2 main goals of evaluating previous ground effect theory and developing the optimum flight profile for maximum range, a computer simulation of the glider was developed and 4 types of flight tests were flown using 3 classes of instrumentation. This approach was designed to maximize flight safety and provide several methods of obtaining data in the event that one method failed. This approach was approved by the Air Force

Flight Test Center (AFFTC) safety review board with some flight limitations on 20 September 1988. Our approach to the simulation and flight tests are covered in this section; the instrumentation is covered in the last section of this chapter.

The glider simulation was developed to increase flight safety, assist in flight test planning, and provide the optimum flight profile for maximum range. The glider simulation used the simplified longitudinal equations of motion in a 3 degree of freedom visual simulation of glider motion as discussed in Chapter III. The simulation was first developed with previously determined drag data on the Grob G-103 glider and Hoerner's ground effect theory. The simulation was later updated with revised Grob G-103 drag data, flight test data on the Let L-13 Blanik, ground effect flight test results, and a National Aeronautics and Space Administration (NASA) atmospheric model giving the reduction in wind velocity with altitude AGL. The glider simulation increased flight safety and assisted in flight test planning by familiarizing the pilots with the flight profiles beforehand, by adjusting the flight test profiles to keep them safely within the performance capabilities of the glider, and by giving information on how to arrange the flight test course and instrumentation. The simulation was used to develop the optimum flight profile for maximum range by using the steepest gradient algorithm and Newton's method

for non-linear systems to optimize 2 flight parameters which a pilot could control during the profile. The simulation is discussed in Chapter III and the profile optimization is discussed in Chapter VI.

A total of 122 test sorties were flown in the Grob G-103 and Let L-13 Blanik gliders between 21 September and 25 October 1988. Four types of flight tests were performed: instrument calibration tests, drag polar tests, level deceleration tests, and flight profile tests. The instrument calibration tests were flown to calibrate the Grob airspeed indicator, since accurate measurement of airspeed is critical to drag determination. The aircraft drag polar tests yielded the Grob drag polar, which represents the variation of drag with lift. This was determined out of ground effect to set a baseline aircraft drag at given flight conditions. Level deceleration tests were then flown at 2 altitudes out of ground effect for a baseline test and at 6 altitudes in ground effect to measure the amount of drag reduction caused by ground effect. Lastly, profile testing was flown to verify the computer simulation, to test various profiles, and to verify the optimum profile for maximum range in both the Grob G-103 and the Let L-13 Blanik. This series of flight tests provided sufficient data to revise previous ground effect theory and to develop the optimum flight profile for maximizing glide range.

Test Articles and Instrumentation

Two gliders and three classes of instrumentation were used in the flight tests. The Grob G103 glider is a tandem-seat, mid-wing, high-performance sailplane of all-fiberglass construction. The Let L-13 Blanik is a tandem-seat, high-wing, medium-performance sailplane of metal-skin construction. Both aircraft were designed for training, soaring, and simple aerobatics. Detailed descriptions of each aircraft are contained in Appendix A.

Instrumentation used during this test included:

1. Front Cockpit

- Sensitive Airspeed Indicator
- Sensitive G-meter
- Production Altimeter
- Outside Air Temperature Gauge

2. Rear Cockpit

- Differential Pressure Gauge
- Production Altimeter
- Stopwatch
- C-Band Beacon
- Video Recorder

3. Ground

- Portable Weather Station
- Radar Gun
- Space Position Optical and Radar Tracking Radar
- Test Project Speed Course
- Portable Fly-By Towers (2)

Instrument errors for the sensitive airspeed indicator, G-meter and differential pressure gauge were measured by the AFFTC 6520 Test Group Engineering Services (6520 TG/ENIT).

Reference 3 describes all instruments and gives the methods and results of instrument calibrations (3:116-120).

The speed course for the Have Effect project was located along Runway 18/36 of Rogers Dry Lake at Edwards AFB, California. Runway 18/36 is 900 feet wide by 24,000 feet long and has 4 black reference lines painted down its length. Figure 1.1 shows the general layout of the speed course on the runway and the typical sequence of operations along the course. The 6,000 foot long speed course was laid out using one of the black runway reference lines as the course centerline. The course consisted of a series of tethered helium balloons offset 50 feet to one side of the course centerline and spaced at 300 to 600 foot intervals along the course length. These balloons were tethered at a measured height to give a height reference which remained constant during each test run but which could be varied from run to run. Two tower fly-by grids were located on the course to determine the height AGL at which the glider flew on each test run. A portable weather station was also located near the speed course to determine the wind and ambient temperature, and a police radar gun was used as a backup measurement of glider groundspeed on the speed course. Reference 3 describes the speed course and its associated instrumentation more completely (3:110-115).

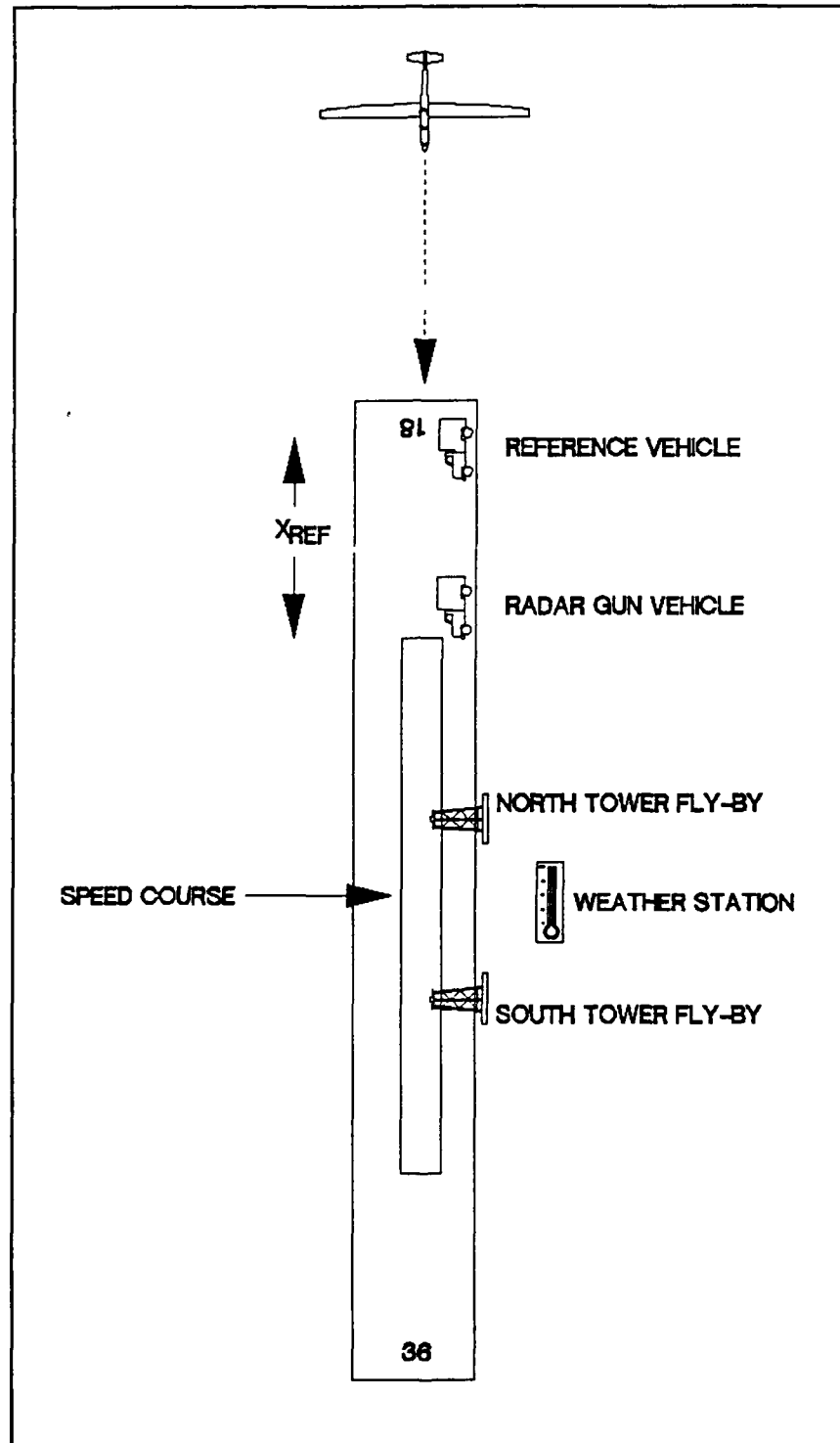


FIGURE 1.1: Speed Course

II. Aerodynamic Theory

Aerodynamics of Drag

The aerodynamics of drag are crucial to understanding how ground effect works. Drag is normally expressed in coefficient form, with the amount of drag being divided by the dynamic pressure and by the wing planform area. Drag can be divided into 4 categories: parasite, induced, wave, and miscellaneous drag (10:4.30). Due to the low speeds and the simplicity of the gliders all drag will be considered to be either parasite or induced drag. The fact that drag data are only of interest during level flight or gentle maneuvers makes these simplifications possible.

Parasite Drag.

Parasite drag does not tend to vary with aircraft lift. It classically consists of drag due to skin friction, pressure differential, and airflow interference. Skin friction drag affects every surface of the aircraft and varies with the Reynolds number of the airflow and with the roughness of the surface. Pressure drag is due to the airflow pressure difference between the forward and aft aircraft surfaces. Pressure drag is primarily caused by airflow separation. Interference drag is caused by the interaction of airflow around nearby external surfaces (10:4.1-4.14, 4.24-4.25).

Induced Drag.

Induced drag is caused by aircraft lift. Assuming that an aircraft derives the majority of its lift from its wing (as most gliders do), a good assumption for the coefficient of induced drag is (10:4.14-4.20):

$$C_{Di} = k C_L^2 \quad (2.1)$$

where:

$$k = \frac{1}{\pi AR e} \quad (2.2)$$

AR is the wing aspect ratio

e is Oswald's wing efficiency factor

Wave Drag.

Wave drag is due to the compressibility of air at high subsonic and supersonic Mach numbers (10:4.26). This drag is not present when the local airflow is less than Mach 1 (10:4.26), and the maximum Mach number reached during the flight tests was only 0.2. Therefore, wave drag will be neglected completely.

Miscellaneous Drag.

Four forms of drag do not fit the other categories of drag and are therefore classified as miscellaneous drag. Ram drag is drag due to air compression in the inlets of powered aircraft (primarily turbojet/turboprop or ramjet

engines) (10:4.27). Ram drag is negligible for gliders due to the lack of a propulsion system. Cooling drag is drag due to energy lost in forcing air through cooling systems. Cooling drag is negligible since the glider cockpit cooling vents were closed on all data runs.

The third form of miscellaneous drag is trim drag, which is the drag created by both the downforce on the horizontal tail and the additional wing lift required to overcome this downforce. This drag may be significant, and it varies primarily with C_L^2 as shown in the drag characteristics estimation section. Because trim drag varies with C_L^2 , it will be included in the induced drag coefficient.

The final form of miscellaneous drag is control drag, which consists of drag due to control inputs and aerodynamic damping. Control inputs create additional drag when the control surfaces deflect and create additional lift forces. This drag due to control inputs was small for the gliders due to the small size of the control surfaces and due to the gentle maneuvers flown which did not require large control surface deflections. The small control inputs made during the flight tests also caused additional drag due to the aerodynamic energy required to dampen the resulting small oscillations of the glider, but this drag was again small due to the gentleness of maneuvering.

Control drag will be considered as being a form of parasite drag since it is only present during maneuvering flight. A control drag coefficient which accounts for the average control drag during gentle maneuvering in level flight will be included in the parasite drag coefficient. Since the control inputs during the gentle flight maneuvers involved in this flight test were small, the deviations from this average coefficient should be negligible.

Conclusions.

For the reasons noted in this discussion, only parasite and induced drag will be considered in this research. Parasite drag will be considered to include skin friction, pressure, interference, and control drag. The parasite drag coefficient C_{D0} will not be considered to vary significantly with C_L . Because C_{D0} is constant, the glider parasite drag will grow with increasing airspeed. Induced drag will include all drag due to lift and trim drag and will be considered to have the form $k C_L^2$. Because induced drag decreases with decreasing C_L , and because C_L decreases with increasing airspeed in steady flight, induced drag will decrease with increasing airspeed. Cooling, wave, and ram drag will be neglected because they are not applicable to the test gliders.

Estimation of Drag Characteristics

Current aircraft design methods were used to estimate the drag characteristics of the Grob and Blanik gliders in order to see how these estimates compared with flight test results. The drag characteristics of the Grob with flaps up and the Blanik with flaps up and down were estimated using the methods described in Reference 8. These methods are currently used for first iteration design estimation and are expected to give first order of magnitude results.

A number of glider characteristics had to be determined in order to make the estimation of drag characteristics. These characteristics and the references from which they were taken are given in Table 2.1.

Estimation of Parasite Drag Coefficient.

The parasite drag coefficient was estimated for the wing, fuselage, horizontal tail, and vertical tail and then combined to give a good estimate of the glider C_{D0} . Control drag was neglected due to the lack of any estimation techniques. Table 2.2 gives the results of the estimations and the results of the out of ground effect flight testing described in Chapter V. The glider parasite drag coefficients matched the flight test coefficients within 19 percent, which is a reasonable estimate.

TABLE 2.1
Glider Characteristics

Characteristic	Grob	Blanik		Reference
		Flaps Up	Flaps Down	
Airfoil	Eppler 603	NACA 63 ₂ A615		13:556 12:750
Surface Material	Polished Fiber-Glass	Polished Aluminum		13:556 12:750
Airfoil Max Thickness	20% c	15% c	15% c	5:143 1:419
Airfoil Max Thickness Location	35% c	35% c	35% c	5:143 1:419
Wing Sweep of Max Thickness	2.7°	-4.1°	-4.1°	3:28-31
Wing Aspect Ratio	17.1	13.7	11.4	3:28-31
Wing Taper Ratio	0.45	0.50	0.45	3:28-31
Mean Aero Chord	3.4 ft	3.9 ft	3.9 ft	3:28-31
Wing Root Chord	4.5 ft	4.5 ft	4.5 ft	3:28-31
Flap Span	--	--	50% b	3:28-31
Fuselage Length	26.8 ft	27.6 ft	27.6 ft	3:28-31
Wing Span	57.4 ft	53.1 ft	53.1 ft	3:28-31
Wing Area (ft ²)	191.6	206.1	248.	3:28-31
Exposed Wing Area-ft ²	171.4	187.2	229.	3:28-31
Horizontal Tail Area	25.8 ft ²	18.4 ft ²	18.4 ft ²	3:28-31
Vertical Tail Area	15.9 ft ²	19.1 ft ²	19.1 ft ²	3:28-31

TABLE 2.2

Estimate of Glider Parasite Drag Coefficients

Parasite Drag Coefficient	Grob	Blanik	
		Flaps Up	Flaps Down
Wing	0.0048	0.005	0.005
Wing Flap	----	----	0.006
Fuselage	0.003	0.0084	0.007
Tails	0.001	0.0009	0.0008
Glider	0.0088	0.0143	0.0188
Flight Test	0.0107	0.012	0.019
Percent Difference	17.8	19.2	1.1

The wing C_{D0} is primarily due to skin friction and can be estimated by the following equation (8:11-13):

$$C_{D0_{wing}} = C_f \left[1 + L \left(\frac{t}{c} \right) + 100 \left(\frac{t}{c} \right)^4 \right] R \frac{2 S_e}{S} \quad (2.3)$$

where

C_f is the turbulent flat plate skin friction coefficient

L is the airfoil maximum thickness parameter

$\left(\frac{t}{c} \right)$ is the airfoil maximum thickness to chord ratio

R is the lifting surface correlation factor

S_e is the wing exposed surface area

S is the wing planform area

The airfoil thickness parameter L was set to 1.2 for both gliders in accordance with Reference 8 due to the locations of the maximum airfoil thickness (8:11-13). The thickness to chord ratio t/c , wing reference area S , and wing exposed area S_e were taken from Table 2-1. The lifting surface correlation factor R was determined from the wing sweep of the line of maximum wing thickness (8:11-14). The turbulent flat plate skin friction coefficient C_f was determined from the wing surface material, the wing mean aerodynamic chord, and a typical flight Reynolds number corresponding to 2300 feet MSL and 60 KTAS for the Grob and Blanik with flaps up or 50 KTAS for the Blanik with flaps down.

An additional drag coefficient $C_{D_{\text{flap}}}$ was added to Blanik with flaps down to account for the added drag of wing flaps. This additional drag coefficient was determined from an empirical relationship shown in Reference 8 (8:9-23).

The fuselage parasite drag coefficient was primarily due to skin friction. Drag due to pressure differential was neglected because both gliders had tapered trailing edges (8:11-23). Drag due to skin friction was estimated using the equation (8:11-24):

$$C_{D_{\text{fuse}}} = C_f \left[1 + \frac{60}{\left(\frac{l_B}{d} \right)^3} + 0.0025 \left(\frac{l_B}{d} \right) \right] \frac{S_{\text{fuse}}}{S} \quad (2.4)$$

where

C_f is the turbulent flat plate skin friction coefficient
and is determined identically to the wing coefficient

l_B is the fuselage length

S_{fuse} is the fuselage wetted area

d is the fuselage equivalent diameter, $\left(\frac{S_{fuse}}{0.7854}\right)^{0.5}$

The parasite drag coefficients of the horizontal and vertical tails were estimated as if these surfaces were similar to the wings. This simplistic assumption is commonly used and results in a good first order approximation (8:12-4). The following equation is therefore used to approximate C_{Do} for the horizontal and vertical tails (8:12-4):

$$C_{Do_{tails}} = C_{Do_{wing}} \left(\frac{S_{vert} + S_{horiz}}{S} \right) \quad (2.5)$$

where

S_{vert} is the vertical tail area

S_{horiz} is the horizontal tail area

Estimation of Induced Drag Factor.

The induced drag factor k_0 (out of ground effect) for the entire glider was estimated as being the wing k_0 . This in effect assumes that the fuselage k_0 is equal to the wing k_0 , and this assumption is good for a first order estimate

(8:11-7). Also, the aircraft trim drag is assumed to be negligible for a first order analysis since it is typically less than 10 percent of the induced drag (8:22-23).

The wing k_0 was estimated from equation 2.2. Oswald's wing efficiency factor e was estimated from the following equation (8:11-9):

$$e = e' \left[1 - \left(\frac{d}{b} \right)^2 \right] \quad (2.6)$$

where

b is the wingspan

e' is another wing efficiency factor

The e' factor was determined from Reference 8 using the wing taper ratio and the wing sweep angle. Finding e' gave all the information needed to find the wing k_0 .

Table 2.3 shows the induced drag estimates developed and the flight test results of Chapter V. The induced drag estimates are within 16 percent of flight test results for both gliders with flaps up. The drag estimate is 43 percent below the Blanik flaps down results, and this is probably due to the fact that the estimation methods did not account for the uneven lift distribution caused by flaps (8:11-10).

Conclusions.

These estimation methods are used for first iteration

TABLE 2.3

Estimate of Glider Induced Drag Factors

Induced Drag Factor	Grob	Blanik	
		Flaps Up	Flaps Down
Glider	0.0194	0.0242	0.0291
Flight Test	0.0230	0.0420	0.0328
Percent Difference	15.7	42.4	11.3

design estimation and are expected to give first order of magnitude results. The methods did provide a parasite drag coefficient estimate within 19 percent of the flight test derived coefficient, but the estimated induced drag factor was up to 43 percent less than the flight test factor. The discrepancy in the induced drag factor was probably due to the fact that the methods in Reference 8 were developed primarily for powered aircraft with aspect ratios below 6; these gliders had aspect ratios ranging from 17.1 to 11.4.

Ground Effect Theory

Aerodynamically, flying close to the ground has the effect of reducing the shape and strength of an aircraft's wingtip vortices. This aerodynamic effect causes a reduction in induced drag, and hence allow cause a glider to fly farther in ground effect. Hoerner has developed theoretical predictions of the amount of induced drag

reduction caused by ground effect (6:20-8), and evaluating his predictions was a major goal of this research.

Lifting Line Theory.

Hoerner developed his theoretical predictions of ground effect using a lifting line theory. This theory predicts the amount of lift a wing will create by modeling the wing as a rotating cylinder moving through the air at the aircraft airspeed as shown in the top half of Figure 2.1. The rotating cylinder develops lift because of the pressure differential between the upper and lower airflows, but it also causes downwash because the momentum of the air is deflected downward. When the rotating cylinder is finite in length, air moves from the high pressure lower airflow out and around the tips of the cylinder (wing) and starts a tip vortex which travels rearward and downward from the surface. A tip vortex theoretically continues infinitely unless it strikes the ground or another vortex, in which case it either dissipates at the ground or interacts with the other vortex. Lifting line theory has been verified in wind tunnels for straight wing aircraft and is useful for analyzing conventional gliders.

Hoerner used the lifting line theory to analyze ground effect by considering an aircraft and its mirror image as shown in Figure 2.1. He modeled the aircraft wing as a rotating cylinder flying at a specified height above ground

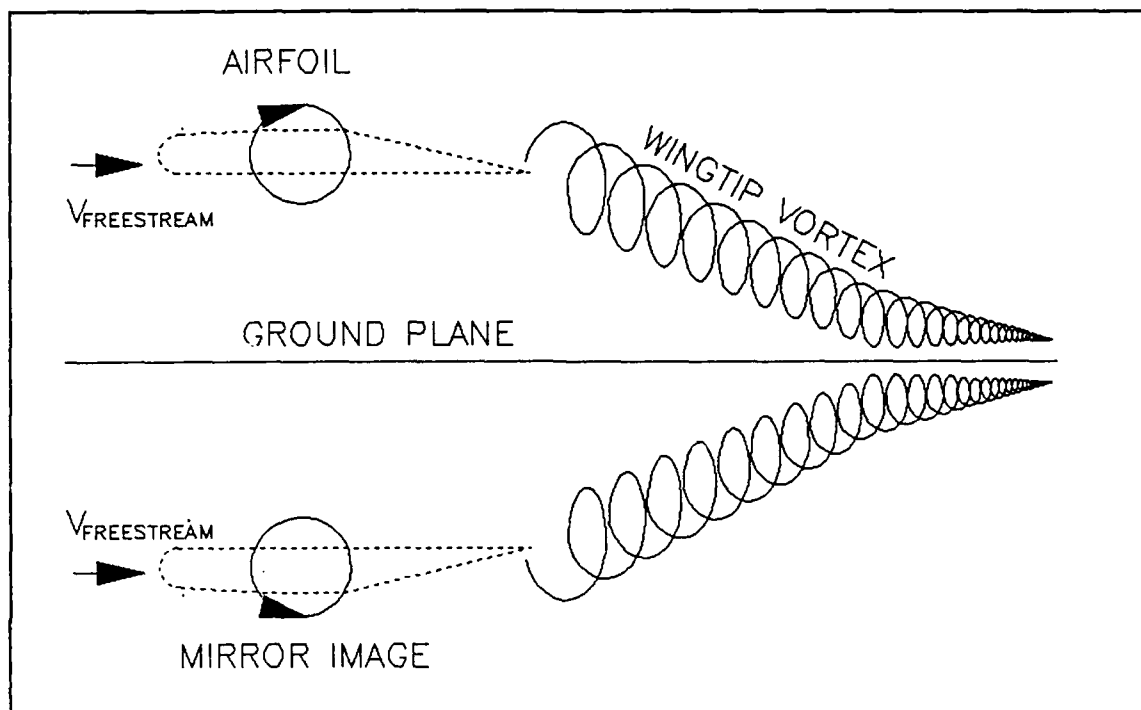


FIGURE 2.1: Lifting Line Theory of Ground Effect

level and then placed another identical rotating cylinder at the same distance below ground as if it were flying upside down. This analysis provides for the interaction of downwash and tip vortices from the rotating cylinder and its mirror image. It also ensures no mass flow through the ground plane due to the symmetry between the cylinder and its mirror image. Because both the downwash and the tip vortices interact, there are 2 different effects predicted (6:20-8 to 20-10).

The first effect predicted by the lifting line analysis is that the lift of the 2-dimensional wing section will be

increased. This effect is caused by the reduction in downwash and subsequent increase in lower airflow pressure caused by the image and is predicted to exponentially increase at heights below half the mean aerodynamic chord (\bar{c}). At heights above half \bar{c} the effect would be insignificant (6:20-10). Since even a low-winged glider such as the Grob has a wing \bar{c} of about 36 inches and sits about 20 inches above ground when resting on its main wheel, the downwash effect on 2-dimensional flow will always be insignificant.

The second effect predicted by the lifting line theory is that the tip vortices will not be as strong, and that induced drag will be reduced. When the tip vortices of the rotating cylinder interact with the vortices of the mirror image, they lose strength and smoothly stop flowing downward. The effect of these reduced strength vortices is to increase the amount of lift the wing provides. To provide the same amount of lift, a wing in ground effect can fly at a lower angle of attack than a wing out of ground effect. This reduced α and the reduced strength of the tip vortices also causes a reduction in the amount of induced drag. The amount of reduction of induced drag is shown in Figure 2.2 (6:20-10).

The amount of drag reduction caused by ground effect

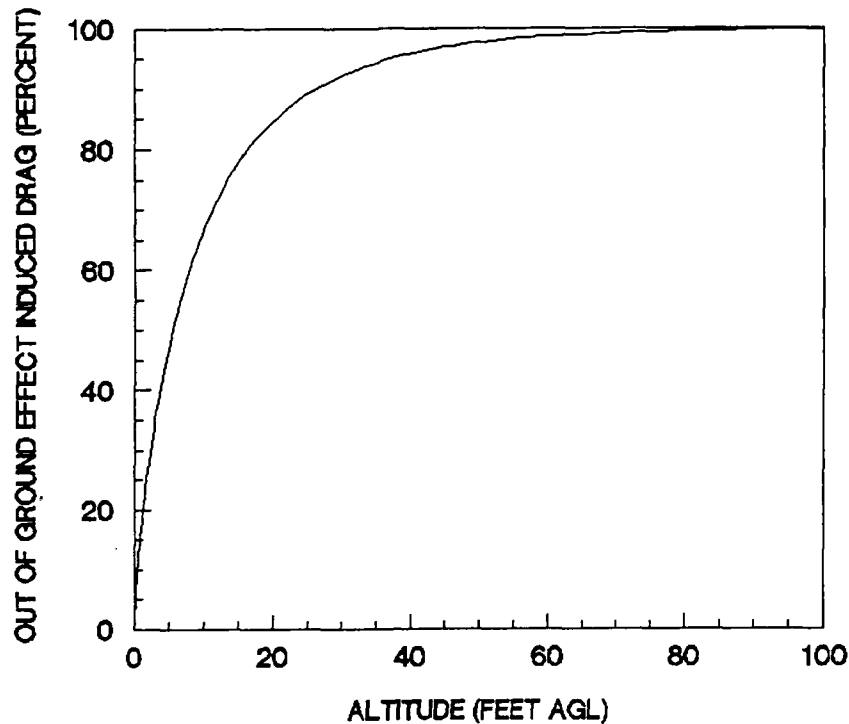


FIGURE 2.2: Predicted Reduction in Gross Induced Drag Due to Ground Effect

can also be expressed by the factor F in the following equation (6:1):

$$F = 1 - \exp[-2.48 (2 h/b)^{0.768}] \quad (2.7)$$

where

h is the height above the ground plane

b is the wingspan

This equation, developed by Dr. Mark Drela of the Massachusetts Institute of Technology for the Daedalus man-powered flight project, is a curve fit to the results of

Hoerner. This equation forms the basis for our predictions of ground effect drag reduction by relating the in ground effect induced drag factor k to the out of ground effect factor k_0 as follows:

$$k = F k_0 \quad (2.8)$$

Ground Effect Ramifications.

An interesting aspect of ground effect is that it depends strictly on the altitude AGL to wingspan ratio as shown in Equation 2.7. The reduction of total aircraft drag depends heavily on the aircraft drag polar characteristics, however. Because induced drag makes up the largest portion of the total aircraft drag at low airspeeds, ground effect is most effective at reducing aircraft total drag at low speeds and is much less effective at high speeds. Figure 2.3 was developed using the drag polar of a Grob and equation 2.7. It illustrates the fact that ground effect reduces drag more at low speeds and low heights.

Atmospheric Wind Model

An atmospheric wind model was developed in order to analyze the effects of winds on the optimum glider flight profile for maximum range. This model of the wind profile assumes that the wind has no vertical component and is valid

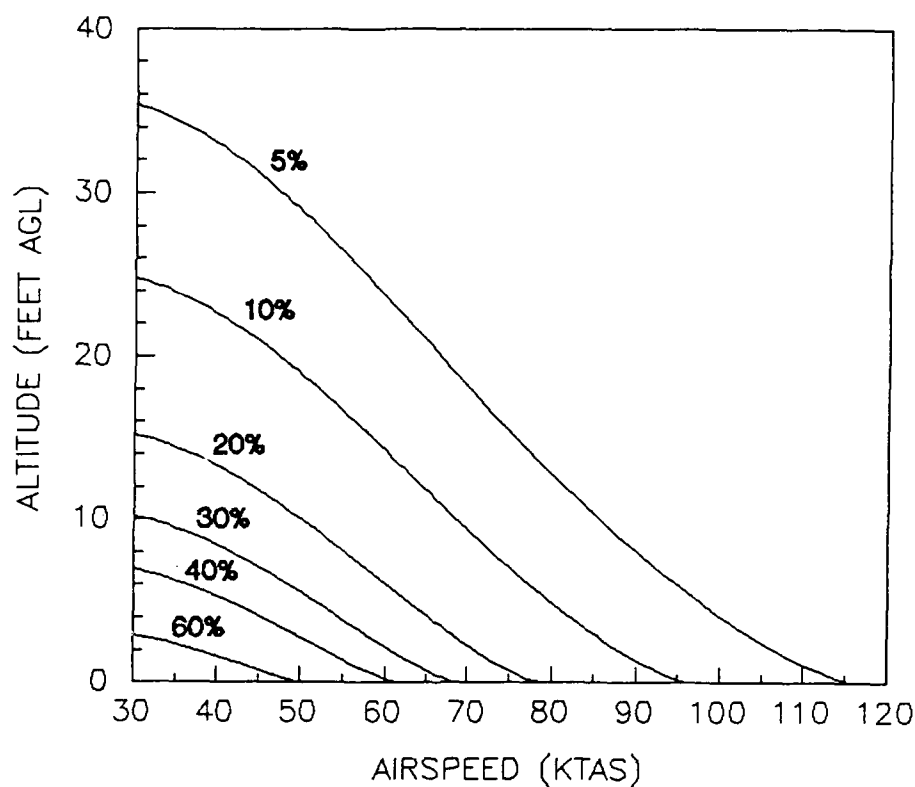


FIGURE 2.3: Predicted Reduction in Grob Total Drag Due to Ground Effect

for atmospheric conditions which have some random turbulence but no significant local updrafts or downdrafts.

Essentially, this model describes a turbulent boundary layer in which wind speed varies logarithmically with height above ground and depends on surface features, boundary layer thickness, and wind speed at the top of the boundary layer.

A representative boundary layer thickness of 900 feet was chosen since most glider pilots begin to look for a specific landing site near this height AGL. The surface roughness of a grassy field was chosen because many gliderports are surrounded by grassy fields, golf courses, or agricultural

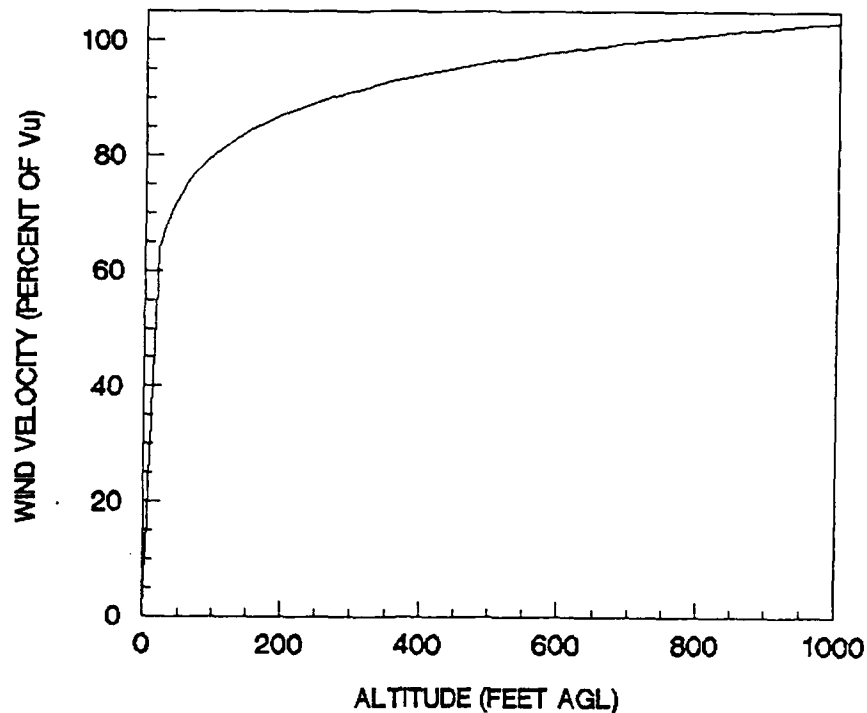


FIGURE 2.4: Wind Model Profile

fields. The wind velocity within the boundary layer V_w at a given height AGL of h can be expressed as (9):

$$V_w = \frac{V_u}{10} \ln(30.48 h) \quad (2.9)$$

where V_u is the velocity of the wind at 900 feet AGL.

Figure 2.4 shows the wind model velocity profile. At $h = 10$ feet, V_w is about half of V_u . At this height, ground effect has significantly reduced the wind gradient, and ground effect reduces the wind gradient even further with small decreases in altitude. When ground effect's promise

to reduce wind velocity by half or more is combined with its promise to reduce total aircraft drag substantially, the potential for lengthening a glide in ground effect is apparent.

III. Simulation

A 3 degree of freedom visual simulation of glider flight was developed for flight planning, drag data reduction, and developing the optimum flight profile for maximum glide range. The simulation was developed from 4 equations of motion, and the simulation was shown to be accurate during the flight tests described in Chapter V.

Equations of Motion

Four kinematic equations of motion were used to model glider longitudinal motion. These 4 equations were derived after making 9 assumptions, and these equations were used in a 3 degree of freedom visual simulation of both test gliders.

Assumptions.

In developing the equations of motion, 9 assumptions were made and were justified as follows:

1. The earth is a flat inertial reference frame (7:205). Since the test maneuvers involved in this project cover short times of 2 minutes or less and short distances of 2.5 miles or less, the errors associated with ignoring the curvature and planetary movement of the earth are insignificant.
2. The atmosphere maintains uniform properties

throughout each test maneuver (7:252). This assumption is very accurate for these tests because the test maneuvers did not have more than 500 feet change in altitude.

3. The test aircraft is a rigid body (7:204). For the gradual maneuvers involved in this test the test aircraft did not experience significant structural bending or changes in any steady state structural bending.

4. The test aircraft is symmetric about the X-Z body axis plane (7:220). The test gliders are very close to being left-right symmetric.

5. The test aircraft mass, center of gravity, and moments of inertia are constant (7:217). The test gliders were ballasted when different aircrew flew to maintain constant mass, center of gravity, and moments of inertia.

6. The test aircraft is flown in nearly steady state flight with no roll or yaw rates, no sideslip or bank angles, and very small pitch rates (7:247). The glider test pilots maintained wings level through visual reference and no sideslip angle through centering the yaw string. Yaw and roll rates were therefore not input, and pitch rates were very small due to the gradual maneuvers involved in the tests.

7. The glider angle of attack is sufficiently small to use small angle approximations. The angle of attack must be small enough that $\cos(\alpha) = 1$ and $\sin(\alpha) = 0$. The maximum α predicted for these tests is only 4 degrees, and the small

angle approximations hold to within 0.07 at 4 degrees α .

8. Longitudinal and lateral-directional aircraft motions are decoupled (7:246). This assumption is reasonable due to the small angles of attack involved and due to the lack of lateral-directional control inputs or aircraft motion during the test maneuvers.

9. The aerodynamic forces and moments acting on the aircraft depend only on the aircraft linear and angular velocities' with respect to the surrounding atmosphere. This assumption neglects the effects of atmospheric disturbances except for random, unbiased turbulence and a constant, steady wind. This assumption is reasonable for the non-turbulent atmospheric conditions which were present for all flight tests and for the random turbulence included in the glider simulation.

Equations of Motion Development.

From the kinematics of Figure 3.1, 4 equations of motion were developed. Dividing the glider velocity into vertical and horizontal components yields equations 3.1 and 3.2 below. Summing forces in the axis tangential to the relative wind (axis t) yields equation 3.3, and summing forces in the axis normal to the wind (axis n) yields equation 3.4.

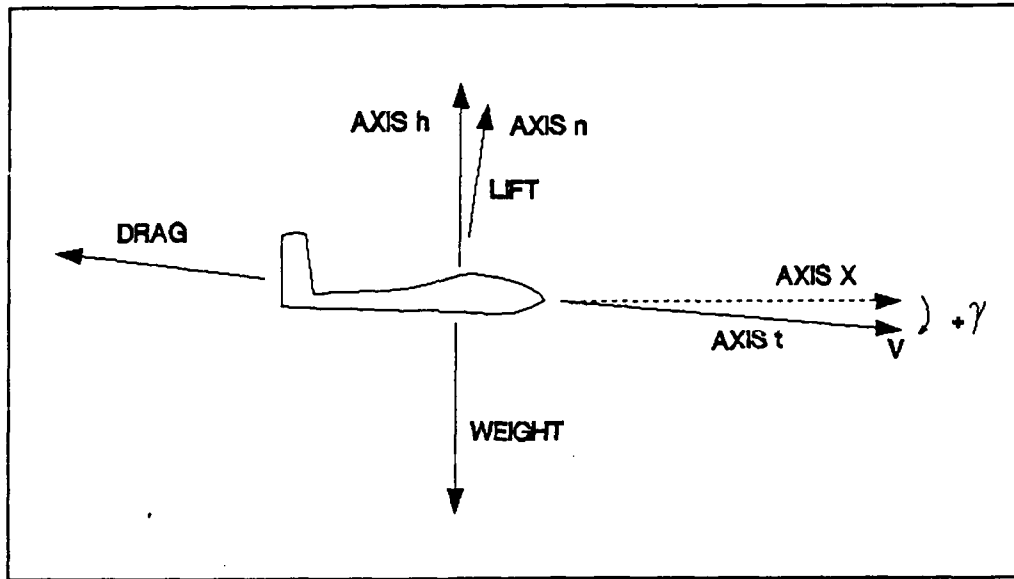


FIGURE 3.1: Glider in Near Steady Flight

$$\frac{dh}{dt} = -V \sin(\gamma) \quad (3.1)$$

$$\frac{dx}{dt} = V \cos(\gamma) \quad (3.2)$$

$$m a_t = m \frac{dV}{dt} = W \sin(\gamma) - D \quad (3.3)$$

$$m a_n = -m V \frac{d\gamma}{dt} = n W - W \cos(\gamma) \quad (3.4)$$

where

$$n = \frac{L}{W} \quad (3.5)$$

These 4 equations adequately describe the longitudinal motion of a glider in near steady flight while undergoing gentle longitudinal maneuvers. These 4 equations form the basis for the 3 degree of freedom simulation, the drag data reduction algorithms, and the flight profile optimizations.

Glider Simulation

A 3 degree of freedom glider simulation was developed based on the equations of motion just derived. The simulation was used in flight planning, in determining the Grob drag polar in ground effect, and in developing the optimum flight profiles for maximum range with and without wind. The glider simulation used the 9 assumptions listed in the equations of motion section and the lifting line model of ground effect. When dealing with winds, the simulation used the turbulent boundary layer wind model derived in the atmospheric wind model section. As is shown in Chapter V, the glider simulation accurately modeled both test gliders during the test maneuvers.

The simulation development begins with the 4 kinematic equations of motion 3.1 through 3.4. These equations relate the motion of a glider through the surrounding atmosphere. In order to account for a steady wind, equation 3.2 is modified as shown below:

$$\frac{dx}{dt} = \left[V - \frac{V_u}{10} \ln(30.48 h) \right] \cos(\gamma) \quad (3.6)$$

where V_u represents the speed of a constant headwind at 900 feet AGL. Having now taken the atmospheric movement into account, the earth fixed set of coordinates as shown in Figure 3.1 will now be used.

The simulation was developed with fixed initial

conditions and one control variable. The starting position, altitude, velocity, flight path angle, and load factor were fixed at specified constants. The control variable was the load factor, which was the only variable which the pilot used for control during the flight tests.

The primary objective of the simulation is to obtain ground velocity and position of the glider as a function of time. Consequently, equation 3.3 will be developed further. Expanding the drag term to its components of parasite and induced drag yields:

$$m \frac{dV}{dt} = W \sin(\gamma) - \frac{1}{2} \rho V^2 S [C_{D0} + k C_L^2] \quad (3.7)$$

From the definition of n in equation 3.5, a substitution for C_L will now be made in equation 3.7:

$$m \frac{dV}{dt} = W \sin(\gamma) - \frac{1}{2} \rho V^2 S \left[C_{D0} + k \left(\frac{2 n W}{\rho V^2 S} \right)^2 \right] \quad (3.8)$$

Next, the lifting line estimate of drag reduction due to ground effect will be factored in. The induced drag factor k will now be broken down from equation 2.8 as:

$$k = k_0 \left\{ 1 - \exp[-2.48 (2 h/b)^{0.768}] \right\} \quad (3.9)$$

where k_0 is the induced drag factor out of ground effect. Making this substitution in equation 3.8 yields:

$$m \frac{dV}{dt} = W \sin(\gamma) - \frac{\rho V^2 S}{2} C_{Do} - k_0 \frac{2 n^2 W^2}{\rho V^2 S} \left\{ 1 - \exp[-2.48 (2h/b)^{0.768}] \right\} \quad (3.10)$$

Equation 3.10 represents a first order inseparable differential equation because γ , h , and n are functions of time. An interesting subset of equation 3.10 occurs during a level deceleration when $\gamma = 0$, $n = 1$, and h is constant. Although the resulting equation could be separated and integrated, it is much easier to integrate numerically. To prove that equation 3.10 is easier to integrate numerically, it will be separated and integrated first. The separated equation is shown below:

$$\frac{v^2 dv}{\frac{\rho S C_{Do} v^4}{2m} + \frac{2 k_0 W g}{\rho S} \left\{ 1 - \exp \left[-2.48 \left(\frac{2h}{b} \right)^{0.768} \right] \right\}} = - dt \quad (3.11)$$

Integrating equation 3.11 with respect to time yields:

$$\left\{ \frac{m}{2 \rho S C_{Do} z} \left[-\ln \left(\frac{v^2 - 2 z v + 2 z^2}{v^2 + 2 z v + 2 z^2} \right) + \tan^{-1} \left(\frac{2 z v}{2 z^2 - v^2} \right) \right] \right\} \Big|_{v_0}^v = t_0 - t \quad (3.12)$$

$$\text{where } z = \left\{ \frac{k_0 W^2 \left\{ 1 - \exp \left[-2.48 \left(\frac{2h}{b} \right)^{0.768} \right] \right\}}{\rho^2 S^2 C_{Do}} \right\}^{0.25}$$

Equation 3.12 cannot be solved in closed form for V . Although equation 3.12 could be solved numerically, numerically integrating equation 3.10 is much simpler. We will now return to the development of the general flight profile where γ , h , and n are free to vary as functions of time.

For an arbitrary flight maneuver where γ , h , and n vary as functions of time, there is no choice but to integrate the 4 kinematic equations of motion numerically. The following equations were used to numerically integrate equations 3.4, 3.10, 3.1, and 3.6 respectively:

$$\gamma_{i+1} = \gamma_i + g \left[\cos(\gamma_i) - n_i \right] \frac{\Delta t}{V_i} \quad (3.13)$$

$$V_{i+1} = V_i + \left\{ g \sin\left(\frac{\gamma_i + \gamma_{i+1}}{2}\right) - \frac{\rho V_i^2 S}{2m} C_{Do} - \frac{2 g k_0 n_i^2 W}{\rho V_i^2 S} \left[1 - \exp\left[-2.48 \left(2 h_i/b\right)^{0.768}\right] \right] \right\} \Delta t \quad (3.14)$$

$$h_{i+1} = h_i - \left(\frac{V_i + V_{i+1}}{2} \right) \sin\left(\frac{\gamma_i + \gamma_{i+1}}{2}\right) \Delta t \quad (3.15)$$

$$x_{i+1} = x_i + \left\{ \frac{V_i + V_{i+1}}{2} - \frac{V_u}{10} \ln\left[30.48 \left(\frac{h_i + h_{i+1}}{2} \right) \right] \right\} \cos\left(\frac{\gamma_i + \gamma_{i+1}}{2}\right) \Delta t \quad (3.16)$$

A forward integration scheme was used on these equations due to the large number of times which they would be used and due to the low level of precision required. Time increments of 0.5 seconds were used for the integrations when γ was constant, and time increments of 0.25 seconds were used when γ was changing. These time increments insured that the numerical errors stayed small enough, especially during flight phases where gradual maneuvering was occurring. The longest simulation made lasted less than 2 minutes, so errors accumulated during the roughly 300 integrations involved were less than the noise in flight test measurements. Up to 67,500 integrations were required of the simulation due to the iterative processes involved in profile optimization, so the simplest and most rapid scheme of forward integration was used.

The integration of these 4 equations yields the position, altitude, velocity, and flight path angle of the glider for all times required. The simulation output was used in 3 different ways. A computer generated visual display of how the simulated flight would look from the glider cockpit used these data in conjunction with speed course setup information. This visual display was not a cockpit simulator in the sense that it did not have cockpit controls; however, the display could show predetermined flight profiles in real time, slow motion, or accelerated time. The visual display was very useful in flight safety

and flight planning; it gave the test pilots a good idea of how the test profile should look, and it helped the test team decide where to place reference balloons on the speed course. The simulation was also used in determining the Grob drag polar in ground effect and the optimum flight profiles for maximum range with and without wind. These uses are discussed in Chapters V and VI.

IV. Optimization Theory

Five optimization algorithms were used in the course of this project to determine numerical solutions to problems which could not be solved in a closed form. The 5 optimization algorithms were used specifically in the glider simulation, in-ground effect drag data reduction, and in optimizing flight profiles for maximum range with and without wind. The 5 optimization algorithms are: Secant, Steepest Gradient, Quadratic Spline Interpolation, Newton's Method for Nonlinear Systems, and Gauss-Newton.

Secant Algorithm

The secant approximation to the Newton-Raphson algorithm was used within the glider simulation to estimate the proper height at which to begin pulling out of a dive in order to arrive at the proper level deceleration altitude. The algorithm approximates solutions to single variable nonlinear functions and is much more computationally efficient than the Newton-Raphson algorithm upon which it is based (2:42-48).

The Newton-Raphson algorithm can be developed using a Taylor series approximation to the nonlinear single variable function $f(x) = 0$. By assuming that an initial guess x_i exists which is close enough to the real solution, second degree and higher terms in the Taylor series can be ignored.

The resulting equation gives an approximate solution x_{i+1} of:

$$x_{i+1} = x_i - \frac{f(x_i)}{f'(x_i)} \quad (4.1)$$

where $f'(x_i)$ represents $d[f(x_i)]/dx_i$. The Newton-Raphson algorithm results when this process is continued iteratively. The algorithm provides better solutions at each iteration (2:42-48).

The secant approximation to the Newton-Raphson algorithm approximates the derivative $f'(x_i)$ in equation 4.1 as follows (2:47):

$$f'(x_i) = \frac{f(x_i) - f(x_{i-1})}{x_i - x_{i-1}} \quad (4.2)$$

The secant algorithm reduces the number of computations required to determine f' . Thus, the complete secant algorithm is expressed in equation 4.3 (2:47).

$$x_{i+1} = x_i - \frac{f(x_i) (x_i - x_{i-1})}{f(x_i) - f(x_{i-1})} \quad (4.3)$$

In the simulation, x represents the altitude at which the pullout starts and $f(x)$ represents the difference between the computed and desired level deceleration altitudes. The objective of the secant algorithm is to

estimate the proper altitude x such that the pullout ends at the desired level deceleration altitude. The simulation recomputes the pullout phase and estimates a new pullout start altitude iteratively until the computed and desired level deceleration altitudes match within 0.2 feet. This match is sufficient since it is better than a human pilot could achieve.

Steepest Gradient Algorithm

The steepest gradient algorithm was used for in ground effect drag data reduction and for developing optimum flight profiles to maximize range with and without wind. In both cases the algorithm was used to optimize nonlinear functions of 2 variables. The steepest gradient algorithm is similar to the Newton-Raphson algorithm in that it uses first derivative information to approximate solutions to nonlinear functions, but the algorithm may be used on multivariate functions.

The steepest gradient algorithm minimizes a function $g(x,y)$ by determining the vector gradient of g (∇g) with respect to x and y :

$$\nabla g = \begin{bmatrix} \partial g / \partial x \\ \partial g / \partial y \end{bmatrix} \quad (4.4)$$

A forward difference formula is used to approximate the partial derivatives $\partial g / \partial x$ and $\partial g / \partial y$ for the gradient at the

i-th iteration of the algorithm as follows:

$$\frac{\partial g}{\partial x} = \frac{g(x_i + \Delta x, y_i) - g(x_i, y_i)}{\Delta x} \quad (4.5)$$

$$\frac{\partial g}{\partial y} = \frac{g(x_i, y_i + \Delta y) - g(x_i, y_i)}{\Delta y} \quad (4.6)$$

where Δx and Δy represent small changes in x and y respectively. The forward difference approximation is used to approximate the gradient because it requires the least number of time consuming functional evaluations. The approximation worked acceptably in the steepest gradient algorithm because the algorithm generates only rough solutions and a small degree of error in the gradient did not affect convergence.

Since g is a function of the 2 variables x and y , the gradient ∇g represents the direction in the 2 dimensional space (x, y) in which g increases most. The steepest gradient algorithm begins with an initial guess (x_i, y_i) and, in order to minimize g , the algorithm computes the next estimate (x_{i+1}, y_{i+1}) in the negative gradient direction as follows:

$$\begin{bmatrix} x_{i+1} \\ y_{i+1} \end{bmatrix} = \begin{bmatrix} x_i \\ y_i \end{bmatrix} - d \nabla g \quad (4.7)$$

The scalar d in equation 4.7 represents the step size taken in the negative gradient direction and is determined using

the quadratic spline interpolation algorithm covered in the next section. Iterations of the steepest gradient algorithm continue until g is sufficiently small.

The steepest gradient algorithm was used in both drag data reduction and in developing optimum profiles. In drag data reduction, the algorithm minimized the cost function C which measured the match between the glider simulation and radar tracking data. The algorithm was also used to maximize the ground distance X covered by the final glider simulation with and without wind. The algorithm required a number of iterations to achieve close solutions, but it provided converging solutions in every case regardless of the value of the starting guesses of the independent variables.

Quadratic Spline Interpolation

The quadratic spline interpolation algorithm was used in the steepest gradient algorithm to determine the best step size to take in each iteration and in the glider simulation to determine the penetration airspeed. The use of the quadratic spline algorithm in the 2 dimensional steepest gradient algorithm will be discussed first; the application to the 1 dimensional problem of finding the penetration airspeed is simpler and follows easily from the 2 dimensional application. The quadratic interpolation algorithm matches a quadratic curve to 3 points lying in the

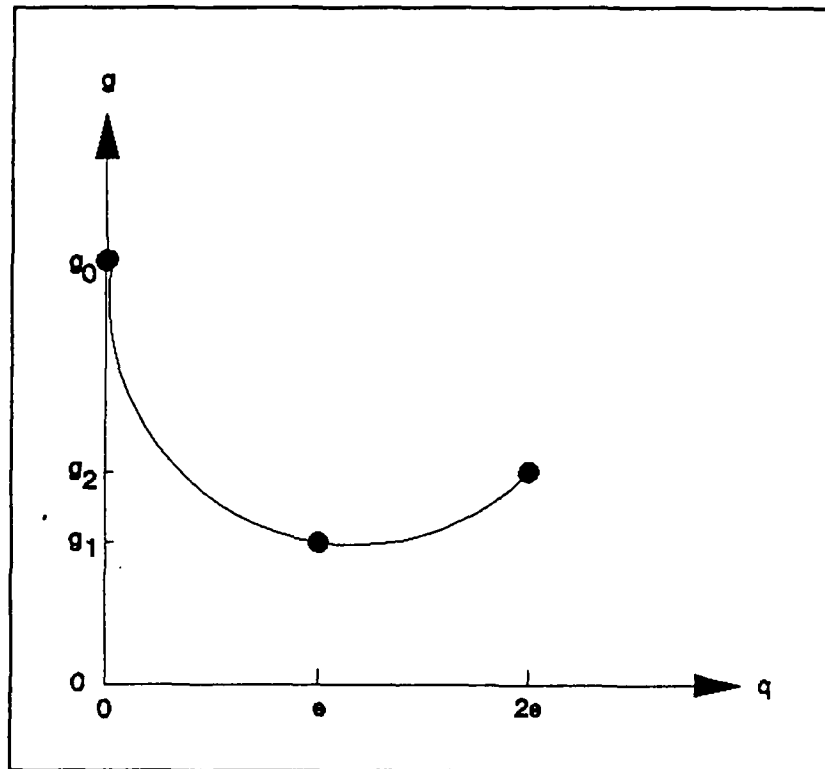


FIGURE 4.1: Quadratic Spline Interpolation

gradient direction of a function and then approximates the minimum of the function as being the minimum of the quadratic curve (2:118). A test of curve points was used to insure that the quadratic curve was convex so that a minimum would occur.

The quadratic spline algorithm begins with the starting guess (x_i, y_i) , the value of $g(x_i, y_i)$, and the value of the gradient $\nabla g(x_i, y_i)$. Two more evaluations of g are then required at small distances e and $2e$ from the starting guess (x_i, y_i) in the negative gradient direction as shown in

Figure 4.1. Since the points g_0 , g_1 , and g_2 in Figure 4.1 now depend only on their distance from g_0 (axis q), a quadratic spline depending only on q is then fitted to these three points. The spline has the form

$$g = a q^2 + b q + c \quad (4.8)$$

where the constants a , b , and c are determined from the values of e , g_0 , g_1 , and g_2 .

The quadratic spline may be either convex, concave, or linear, depending on the values of g_0 , g_1 , and g_2 . In order to find a minimum of the spline, the spline must be convex. Choosing the proper value of e will insure that the spline is convex. Since g_1 is in the negative gradient direction from g_0 , a small enough value of e will insure that $g_1 < g_0$. In the actual algorithm used, a small but arbitrary value of e was first used and the value of e was halved repeatedly until g_1 was less than g_0 . Once $g_1 < g_0$, the spline will now be convex if $g_2 > g_1$. If $g_2 < g_1$, the value of e was doubled repeatedly until $g_2 > g_1$. This process gave a convex spline in all cases until the limits of machine precision were reached.

Having created a convex spline, the minimum of the spline will now be found as the best point to begin the next steepest gradient iteration. The minimum of the spline is found simply by differentiating the spline equation 4.8 with

respect to q . This yields:

$$q_{\min} = - \frac{b}{2a} \quad (4.9)$$

The value of q_{\min} represents the distance to move in the negative gradient direction from g_0 in order to find the minimum value of g . This value of q_{\min} is the step size d in the steepest gradient algorithm (equation 4.7).

The quadratic spline interpolation algorithm was used in every iteration of the steepest gradient algorithm. It gave good results to the limits of machine precision or to the precision limits to which the function could be evaluated.

The quadratic spline algorithm was used similarly to find the penetration airspeed for the glider simulation. As shown in Chapter VI, the algorithm was used to minimize the ground approach angle, maximizing glide range out of ground effect. The ground approach angle γ_{ground} is equivalent to the function g in the previous development, except that g is now a function of the single variable q (the true airspeed V is equivalent to q). The 3 points g_0 , g_1 , and g_2 are found as shown in Figure 4.1, and a quadratic curve is fitted to the function g as defined in equation 4.8. The optimum value of q (q_{\min}) is now computed with equation 4.9, and the next algorithm begins at this point. The algorithm stopped when V changed less than 0.05 knots per iteration, giving a

solution within 0.25 knots of the optimum solution. The algorithm always gave good results in 5 to 8 iterations.

Newton's Method for Nonlinear Systems

Newton's method for nonlinear systems was used in this project for developing optimum flight profiles to maximize range with and without wind. Like the steepest gradient algorithm, it was used to minimize a highly nonlinear function of 2 variables. Newton's method differs from the steepest gradient algorithm in that it uses second derivative information and in that it requires a starting guess sufficiently close to the actual solution for convergence.

Algorithm Development.

Newton's method was developed using a Taylor series expansion for a small area around the minimum of a function as shown in Reference 2. Ignoring third and higher order terms for an arbitrary function $g(x,y)$, the following equation can be derived (2:496-499):

$$\begin{bmatrix} x_{i+1} \\ y_{i+1} \end{bmatrix} = \begin{bmatrix} x_i \\ y_i \end{bmatrix} - [J_i]^{-1} \nabla g_i \quad (4.10)$$

The term ∇g_i represents the gradient of g as defined in equation 4.4 evaluated at the i -th iteration of the algorithm. The term J_i represents the Jacobian matrix of

second partial derivatives defined below evaluated at the i-th iteration of the algorithm.

$$J = \begin{bmatrix} \frac{\partial^2 g}{\partial x^2} & \frac{\partial^2 g}{\partial x \partial y} \\ \frac{\partial^2 g}{\partial y \partial x} & \frac{\partial^2 g}{\partial y^2} \end{bmatrix} \quad (4.11)$$

The Jacobian matrix J_i in equation 4.10 will be positive definite and invertible provided that the function g is convex and provided that the i-th point is sufficiently close to a minimum of g (15:233). The functions dealt with in this project were sufficiently convex near their minima that J was always positive definite and invertible once a suitable starting point was found.

Jacobian Approximation.

The Jacobian matrix J_i in equation 4.10 could not be evaluated in closed form for the functions dealt with in this project. A suitable approximation for the Jacobian matrix was developed using second derivative approximations, however.

Four terms need to be approximated in J as expressed in equation 4.11, but 2 of these terms are equivalent. The terms $\frac{\partial^2 g}{\partial x^2}$ and $\frac{\partial^2 g}{\partial y^2}$ were approximated by the 3 point second

derivative formula developed in Reference 2 as follows

(2:142):

$$\frac{\partial^2 g}{\partial x^2} = \frac{1}{(\Delta x)^2} [g(x_i - \Delta x, y_i) - 2g(x_i, y_i) + g(x_i + \Delta x, y_i)] \quad (4.12)$$

$$\frac{\partial^2 g}{\partial y^2} = \frac{1}{(\Delta y)^2} [g(x_i, y_i - \Delta y) - 2g(x_i, y_i) + g(x_i, y_i + \Delta y)] \quad (4.13)$$

Some development is required to approximate $\frac{\partial^2 g}{\partial x \partial y}$, which is equivalent to $\frac{\partial^2 g}{\partial y \partial x}$. To begin with, a 2 point difference formula is used to approximate $\partial g / \partial x$ as follows (2:138):

$$\frac{\partial g}{\partial x} = \frac{g(x_i + \Delta x, y_i) - g(x_i - \Delta x, y_i)}{2 \Delta x} \quad (4.14)$$

Taking the partial derivative of equation 4.14 with respect to y results in:

$$\frac{\partial^2 g}{\partial x \partial y} = \frac{1}{2 \Delta x} \left[\frac{\partial g(x_i + \Delta x, y_i)}{\partial y} - \frac{\partial g(x_i - \Delta x, y_i)}{\partial y} \right] \quad (4.15)$$

Using the 2 point differentiation approximation on each term on the right side of equation 4.15 then gives (2:138):

$$\begin{aligned} \frac{\partial^2 g}{\partial x \partial y} = & \frac{g(x_i + \Delta x, y_i + \Delta y) - g(x_i + \Delta x, y_i - \Delta y)}{4 \Delta x \Delta y} \\ & - \frac{g(x_i - \Delta x, y_i + \Delta y) + g(x_i - \Delta x, y_i - \Delta y)}{4 \Delta x \Delta y} \end{aligned} \quad (4.16)$$

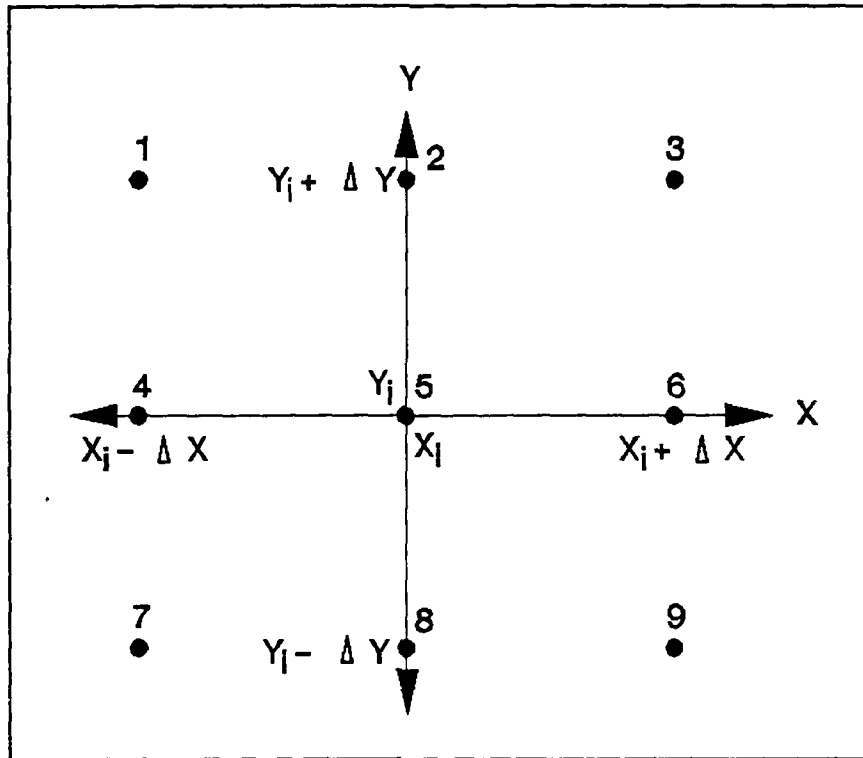


FIGURE 4.2: Points Used in Jacobian and Gradient Approximations

These approximations to the Jacobian matrix require 9 functional evaluations, but they provide a very good approximation to the Jacobian matrix. All terms in the Jacobian matrix are approximated from the 9 points surrounding and including the point of interest as shown in Figure 4.2. The use of points both ahead and behind the point of interest insures a high degree of accuracy (2:140).

Gradient Approximation.

A more accurate gradient approximation was used for Newton's method than for the steepest gradient algorithm.

This more accurate approximation was available due to 2 functional points which had already been evaluated for the Jacobian approximation. The additional points (points 4 and 8 on Figure 4.2) gave information behind the point of interest (point 5) which was not available in the steepest gradient algorithm.

A 2 point difference formula was used to develop the following approximations for $\partial g/\partial x$ and $\partial g/\partial y$ at the i -th iteration of Newton's method (2:138):

$$\frac{\partial g}{\partial x} = \frac{g(x_i + \Delta x, y_i) - g(x_i - \Delta x, y_i)}{2 \Delta x} \quad (4.17)$$

$$\frac{\partial g}{\partial y} = \frac{g(x_i, y_i + \Delta y) - g(x_i, y_i - \Delta y)}{2 \Delta y} \quad (4.18)$$

Equations 4.17 and 4.18 were then used in equation 4.4 to approximate the gradient ∇g . Although this more accurate gradient approximation was not required for convergence or algorithm effectiveness, the approximation did make the Newton algorithm more efficient without any additional computational effort.

Gauss-Newton Algorithm

The Gauss-Newton algorithm is very similar to Newton's method and was used to determine the aircraft drag polar in ground effect. The only differences between the Gauss-Newton algorithm and Newton's method for nonlinear

systems are the ways in which the gradient ∇g (equation 4.4) and the Jacobian matrix of partial derivatives J (equation 4.11) are approximated. The overall Gauss-Newton algorithm is developed exactly the same as shown in the algorithm development subsection of the Newton method.

In the Gauss-Newton algorithm, the gradient was approximated using the forward difference formula (equations 4.5 and 4.6) rather than the 2 point difference formula (equations 4.17 and 4.18) used in Newton's method. This forward difference formula saved 2 lengthy functional computations per iteration and did not significantly degrade algorithm accuracy. In most cases, the Gauss-Newton algorithm with the forward difference formula converged to within 2 decimal places of the final solution in 5 iterations. Increased gradient accuracy might have eliminated 1 or 2 iterations but would have increased the algorithm complexity and the total number of functional computations required.

A unique approximation to the Jacobian matrix J forms the heart of the Gauss-Newton algorithm. The algorithm only works on a function g which is a sum of squared differences, which was the form of the function C in the in ground effect drag polar determination. For the purposes of algorithm development, g will now be defined as:

$$g = \sum_{j=1}^k \left[(p_j - m_j)^2 + 1 (q_j - n_j)^2 \right] \quad (4.19)$$

Where k , l , m , and n are arbitrary constants and p and q are scalars which are functions of x and y . Note that g in equation 4.19 is still only a function of x and y and therefore still works in Newton's method.

Development of the Jacobian approximation begins with taking the partial derivative of equation 4.19 with respect to x_i (the value of x at the i -th iteration of the Gauss-Newton algorithm). This yields:

$$\frac{\partial g}{\partial x_i} = \sum_{j=1}^k \left[2 (p_j - m_j) \frac{\partial p_j}{\partial x_i} + 2 l (q_j - n_j) \frac{\partial q_j}{\partial x_i} \right] \quad (4.20)$$

Taking another partial derivative of equation 4.20 with respect to x_i yields:

$$\frac{\partial^2 g}{\partial x^2} = 2 \sum_{j=1}^k \left[(p_j - m_j) \frac{\partial^2 p_j}{\partial x_i^2} + \left(\frac{\partial p_j}{\partial x_i} \right)^2 + l (q_j - n_j) \frac{\partial^2 q_j}{\partial x_i^2} + l \left(\frac{\partial q_j}{\partial x_i} \right)^2 \right] \quad (4.21)$$

If the point (x_i, y_i) is sufficiently close to a local minimum of g , the second derivative terms of equation 4.21 will be negligible in comparison to the first derivative terms (11:7-13). If the point is not sufficiently close, the Gauss-Newton algorithm may not converge. Once good starting points were found, the Gauss-Newton algorithm converged in all drag data reduction cases.

Neglecting the second derivative terms in equation 4.21

and noting that m and n are always constant yields the approximation to the Jacobian element $\partial^2 g / \partial x^2$ (11:7-14):

$$\frac{\partial^2 g}{\partial x^2} = 2 \sum_{j=1}^k \left[\left(\frac{\partial p_j}{\partial x_i} \right)^2 + 1 \left(\frac{\partial q_j}{\partial x_i} \right)^2 \right] \quad (4.22)$$

The remaining Jacobian terms can be developed similarly and are shown below:

$$\frac{\partial^2 g}{\partial y^2} = 2 \sum_{j=1}^k \left[\left(\frac{\partial p_j}{\partial y_i} \right)^2 + 1 \left(\frac{\partial q_j}{\partial y_i} \right)^2 \right] \quad (4.23)$$

$$\frac{\partial^2 g}{\partial x \partial y} = \frac{\partial^2 g}{\partial y \partial x} = 2 \sum_{j=1}^k \left[\left(\frac{\partial p_j}{\partial x_i} \right) \left(\frac{\partial p_j}{\partial y_i} \right) + 1 \left(\frac{\partial q_j}{\partial x_i} \right) \left(\frac{\partial q_j}{\partial y_i} \right) \right] \quad (4.24)$$

The Gauss-Newton algorithm was effective at finding very precise drag polar solutions in ground effect. The algorithm used semi-second derivative information to achieve this precision without requiring a large number of functional evaluations. The algorithm required a reasonably close starting point which was determined using the steepest gradient method.

V. Flight Test

Overview

Six different types of flight tests were flown during this project. This chapter summarizes the test preparations and the 6 flight tests; Reference 3 gives further information on test preparations, methods, and conduct of all 6 flight tests. The 6 types of flight tests flown were:

1. Pitot-static system calibration.
2. Drag polar out of ground effect.
3. Drag polar in ground effect.
4. Flight profile familiarization.
5. Flight profile development.
6. Flight profile verification.

Test Conditions

The test team took considerable care to insure that the test gliders maintained consistent aerodynamic and inertial qualities throughout the flight tests. Prior to the first test flight of each day, the test glider control surface gaps were retaped and all exterior surfaces were wiped down for consistent drag characteristics. The spoilers were retracted and cockpit vents closed for all flight tests to maintain a consistent aircraft configuration. The weight and center of gravity of the Grob were determined at the AFFTC weight and balance hangar prior to its first flight

test. Subsequent Grob flight tests used ballast to maintain its weight and center of gravity with different aircrews. Only 1 aircrew flew the Blanik, and its weight and center of gravity were determined from the manufacturer's flight manual.

Similar care was taken to insure standardized atmospheric conditions for the flight tests. Outside air temperature and pressure altitude were measured on each test and were used to correct test results to standard day, 2300 feet MSL conditions. The test aircrew terminated flight testing if they felt any atmospheric turbulence, updrafts, or downdrafts. Winds for the out of ground effect drag polar tests were 7 knots or less but did not affect the test data due to the test method involved. Winds for all other flight tests were 2 knots or less.

Initial Tests

A set of ground tests and the first 2 sets of flight tests were performed to calibrate sensitive flight instruments in the Grob. The AFFTC 6520 Test Group Engineering Services installed, calibrated, and measured the instrument errors of three sensitive flight instruments in the Grob: an airspeed indicator, a G-meter, and an airflow differential pressure gauge (used to help calibrate the airspeed indicator). Trailing-cone flight tests were made out of ground effect to determine the static source position

errors of the airspeed indicator. Comparisons of video recorded cockpit airspeed indications with radar tracking velocity data confirmed that these static source position errors did not change in ground effect. The aircraft production altimeter was also effectively calibrated by this test since it is driven by the same static sources as the airspeed indicator. The airspeed indicator, altimeter, and G-meter gave accurate readings during the rest of the flight tests, and the airflow differential pressure gauge was disconnected after this first test.

Following instrument calibration tests, a second set of flight tests were flown to determine the Grob drag polar out of ground effect. Timed constant airspeed glides were flown at 21 different airspeeds ranging from 44 to 110 knots calibrated airspeed (KCAS) and at altitudes ranging from 6,000 to 2,500 feet MSL. The Grob out-of-ground effect drag polar was then determined from the glide ratio during these descents as described in Reference 3 (3:13, 15, 49). Figure 5.1 shows the Grob out-of-ground effect drag polar. The curve is a least-squares fit to the flight test data. The zero lift drag coefficient (C_{D0}) was 0.01065, and the induced drag factor (k_0) was 0.02296.

Drag Polar In-Ground Effect

A series of level decelerations were flown to measure the Grob drag polar in-ground effect. The aircraft entered

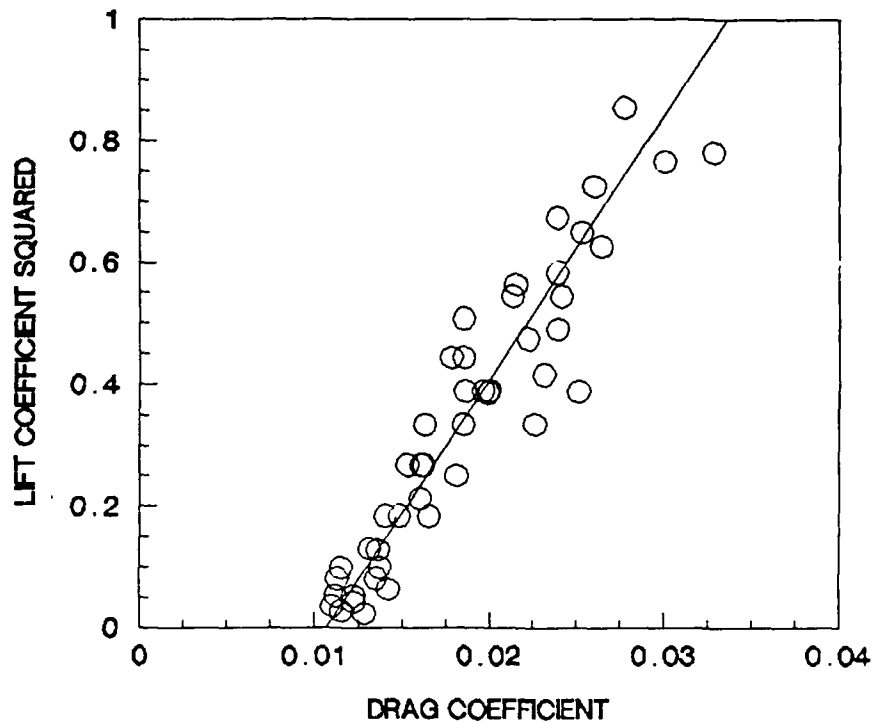


FIGURE 5.1: Grob Drag Polar Out of Ground Effect

the speed course at a set altitude and airspeed. The pilot maintained altitude using tethered balloons as references and continued the level deceleration until the end of the speed course or until his airspeed dropped below 50 KIAS. A cockpit video recorder, a radar gun, two tower fly-by stations, a weather station, and radar tracking instrumentation were used to record data. Radar tracking position and velocity data were used in the drag polar determination because of their high accuracy and high sampling rate of 1 Hertz. The fly-by towers were used to verify the height AGL of each deceleration, and the first set of radar tracking data was qualitatively verified with

video recorder and radar gun data. Wind and air temperature readings were taken at the weather station every second deceleration and interpolated for the readings of each deceleration.

Data Reduction.

To determine the drag reduction due to ground effect, the glider simulation developed in Chapter III was matched to the radar tracking data of each deceleration. The drag parameters C_{D0} and k were varied in the simulation to get the best possible match between the simulation and the radar data. The induced drag factor giving the best match represented the average induced drag factor for that deceleration, and the drag reduction due to ground effect was found by comparing this k to k_0 , the induced drag factor out of ground effect. The parasite drag coefficient C_{D0} was varied in addition to k because the glider control drag varied from data run to data run, and these variations would corrupt the determinations of k if they were not accounted for. The quality of the match between the simulation and radar data was measured by the following weighted sum of squared differences cost function C :

$$C = \sum_{j=1}^N \left[(x_{sj} - x_{rj})^2 + 13.97 (v_{sj} - v_{rj})^2 \right] \quad (5.1)$$

where:

X_{sj} is the simulation ground distance at point j

X_{rj} is the radar data ground distance at point j

V_{sj} is the simulation true velocity at point j

V_{rj} is the radar data true velocity at point j

N is the total number of radar data points

The velocity term in the cost function above was weighted by a factor of 13.97 to account for the greater accuracy of velocity measurements in the radar data. The expected value of the velocity measurement error was ± 2.80 feet per second, 3.74 times less than the expected ground distance measurement error of ± 10.48 feet. Therefore, the squared velocity term in the cost function was weighted by 3.74 squared to weight the more accurate velocity data.

The steepest gradient and Gauss-Newton minimization algorithms were used in combination to minimize the cost function C and achieve a good match between the simulation and radar data. Chapter IV describes these algorithms in detail. The cost function C was equivalent to the function g in Chapter IV, and C was a function of C_{D0} and k , which were equivalent to x and y in Chapter III. On each level deceleration, the steepest gradient algorithm was used for 1 or 2 iterations to find a solution of C_{D0} and k which were relatively close to the best solution. The Gauss-Newton

algorithm was then used for 5 to 10 iterations starting with the steepest gradient solution to find a very precise solution which was within 0.0005 of the best solution.

Results.

The combination of the 2 optimization algorithms gave good results on 29 of the 47 decelerations it was used on. On the 29 decelerations which gave good results, the simulation and the radar data matched well enough that the differences were typically less than 0.5 knots in velocity and 3 feet in ground position at each data point.

The algorithms failed to give good results on 18 of the 47 decelerations due to a convergence to impossible values of C_{Do} and k . The algorithms guarantee that they will converge to a local minimum of the function, but they do not guarantee that this local minimum is the correct solution. Therefore, a reasonableness check was made to insure that C_{Do} and k were within ± 100 percent of Hoerner's predictions. This reasonableness check identified 18 impossible solutions and it made sure that the remaining 29 solutions were reasonable.

Table 5.1 shows the parasite coefficients and induced drag factors at each altitude. The parasite drag coefficients were averaged at each altitude as shown but showed no discernable relationship with altitude. The average parasite drag coefficient for all altitudes was

TABLE 5.1
Ground Effect Drag Parameters

ALTITUDE (feet)	C_{Do}	K	
		AVERAGED TEST DATA	THEORY
100	0.01257	0.02302	0.02291
60	0.01164	0.02327	0.02267
30	0.01171	0.02064	0.02119
20	0.01147	0.01976	0.01945
15	0.01282	0.01731	0.01786
10	0.01188	0.01542	0.01534
6	0.01231	0.01282	0.01206
4	0.01187	0.01154	0.00966

Avg C_{Do} : 0.01192 (11.6% Above Predicted C_{Do} of 0.010675)

0.01192, which is 11.6 percent above the coefficient found during the out of ground effect drag polar flight tests. This additional drag and the variations in C_{Do} between data runs are most likely due to lateral and longitudinal control inputs and the aerodynamic energy required for the aircraft dynamic responses, all of which this analysis assumed to be constant. The increased C_{Do} could also be due to the fact that the task of flying a level deceleration at a precise height AGL is much more demanding than flying a constant airspeed glide out of ground effect. A more demanding task requires larger and more frequent control inputs, generating

more control drag in the deceleration than in a steady glide. This additional parasite drag was incorporated into the level deceleration maneuvers of the revised aircraft simulation. The induced drag may have also varied due to slight variations of height above ground between different decelerations. Ground effect theory predicts that even a 6 inch difference in height could cause up to a 7.5 percent change in induced drag at low altitudes such as four feet AGL. These factors explain why the parasite and induced drag parameters varied from deceleration to deceleration and why C_{D0} in ground effect was larger on average than out of ground effect.

Figure 5.2 shows the theoretical and actual induced drag reduction caused by ground effect. These results show some data scatter due to the reasons previously discussed, but the average of the test data at each altitude matches the theoretical data closely, especially at the higher altitudes. From 100 to 10 feet AGL, the average of the measured induced drag factors falls relatively close to the theoretical predictions. These data therefore verify that the lifting line theory gives good predictions of induced drag reduction due to ground effect in this altitude band.

At 6 and 4 feet AGL, the test data show 8 and 16 percent more drag respectively than the theoretical predictions. This greater induced drag may be due to several reasons. The pilots flying the level decelerations

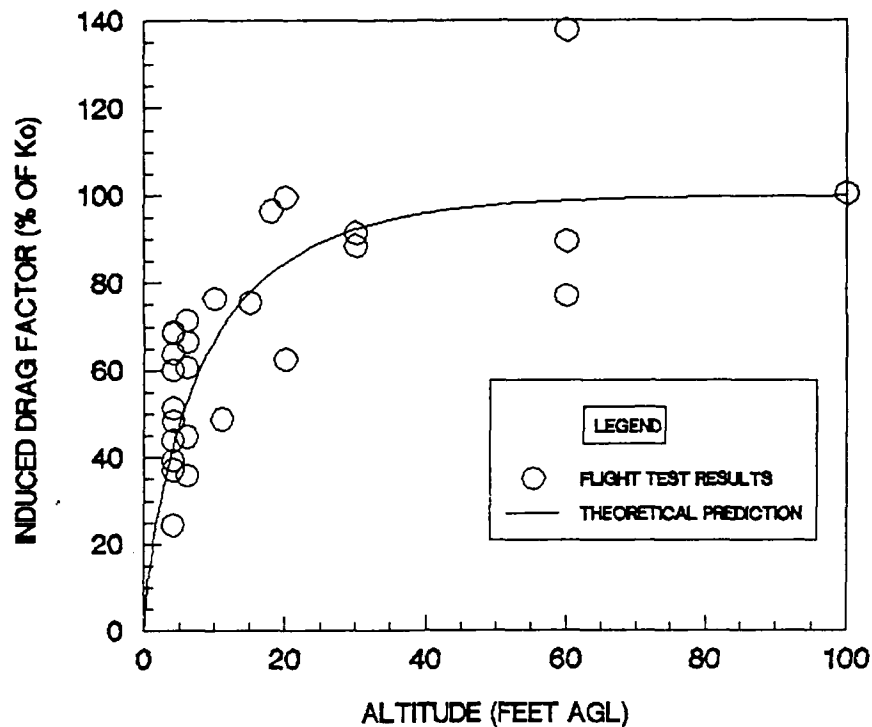


FIGURE 5.2: Ground Effect Drag Reduction

may have flown slightly high on average, since even a 6 inch greater altitude could cause up to 7.5 percent greater induced drag. It is also possible that the radar position and velocity data were biased such that the glider appeared to decelerate more rapidly than it actually did. This is highly unlikely because previous radar error analyses have shown that the radar data does not have biases (14:1) and because the large number of data samples on each deceleration would keep random errors from causing a significant bias. Finally, the test data may be correct and ground effect may not cause as great a reduction in induced drag as predicted. The lifting line theory neglects

viscosity, and viscous effects may alter the aerodynamics of ground effect at low altitudes.

An additional drag due to viscosity makes intuitive sense when the theoretical curve in Figure 5.2 is examined at low altitudes. The theoretical curve predicts that lift can be generated at very, very low altitudes without any drag penalty. Nature never gives us such a "free lunch," and viscosity is a tool nature often uses to spoil a predicted 'free lunch. Thus, viscous effects may have first been significant between 10 and 6 feet AGL and would be expected to grow as altitude decreased. Altitude errors and radar biases may account for some of the difference between the low altitude test data and the theoretical predictions, but the test results are sufficiently good to question the theoretical predictions of ground effect at low altitudes. The real drag reduction due to ground effect at low altitudes therefore probably lies closer to the test data than to the theoretical predictions of the lifting line theory.

While the reasons why ground effect does not provide as large a drag reduction at low altitudes as predicted are not certain, the effect on glider range is. Ground effect has been shown to reduce induced drag, but it did not reduce induced drag as much at low altitudes as predicted. Therefore, a new empirical prediction of ground effect was developed and is shown in Figure 5.3. This empirical ground

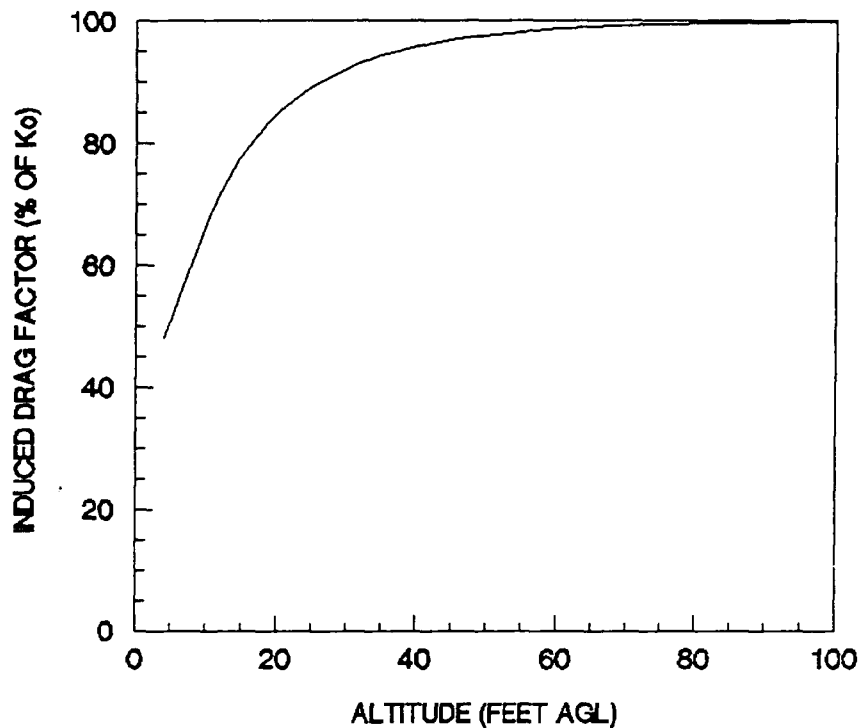


FIGURE 5.3: Revised Ground Effect Drag Reduction Model

effect prediction uses the lifting line prediction of ground effect down to 10 feet AGL and then uses a line drawn through the averaged test data below 10 feet AGL. Note that this new ground effect prediction stops at 4 feet AGL because this is the lowest altitude a glider could fly even in near perfect test conditions. This new ground effect prediction is intended only for glider analyses; the prediction may not be completely accurate aerodynamically, but it will give the correct results for glider performance analyses. This ground effect prediction is incorporated in a revised glider simulation to more accurately reflect the glider performance.

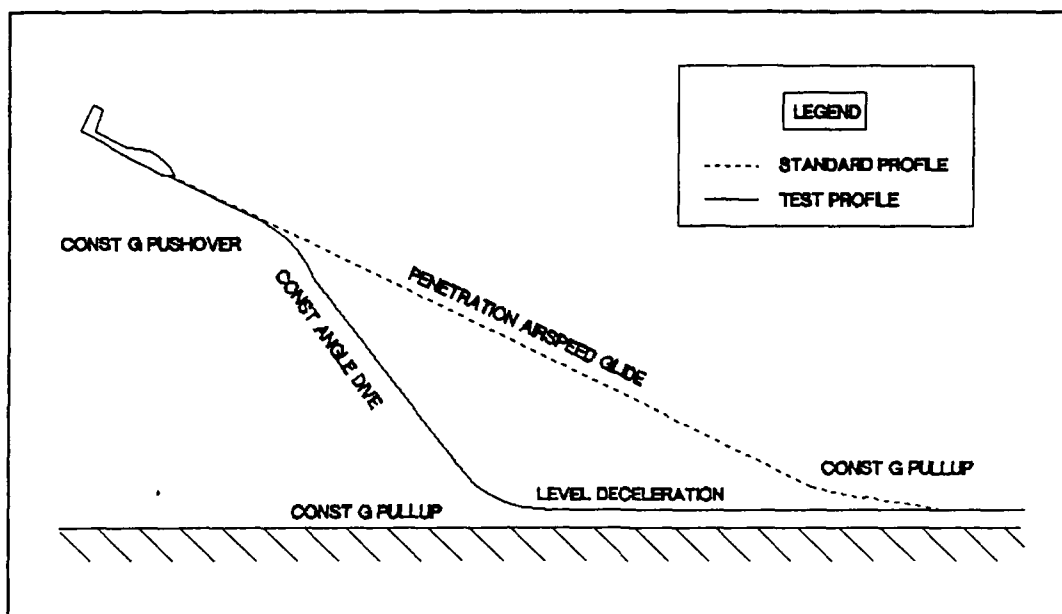


FIGURE 5.4: Standard and Test Flight Profiles

Flight Profile Familiarization

Profile Development.

A test flight profile was developed to test how to best use ground effect to maximize glide range. The test profile consisted of 5 maneuvers, as shown in Figure 5.4. The profile began with a constant airspeed glide at the best penetration airspeed. A constant load factor pushover was initiated at a specified height AGL and held to a planned dive angle. A constant angle dive was then flown to gain airspeed, followed by a constant load factor pullout initiated at a specified height. The final maneuver was a level deceleration. Breaking up the profile into these 5

manuevers allowed the profile to be standardized among test pilots and still provided the maximum flexibility a glider pilot could use in low altitude maneuvering to extend range.

Figure 5.4 also shows the standard 3 maneuver flight profile that glider pilots currently fly to maximize glide range. The standard profile consists of a constant airspeed glide at best penetration airspeed followed by a pullout to a level deceleration in ground effect which is maintained until the glider runs out of airspeed and stalls. The range resulting from this 3 maneuver profile will be the standard against which all test profiles will be evaluated.

The test flight profile began with a constant airspeed dive at the best penetration airspeed because this maneuver maximizes the ratio of groundspeed to vertical velocity and thus maximizes glide range out of ground effect. The best penetration airspeed glide is therefore used to maximize glide range at higher altitudes and is maintained until the optimum altitude to begin a transition into flight in ground effect. Glider pilots are currently taught to fly this airspeed to maximize range, so it is a logical airspeed from which to start.

Given that the test flight profile begins with a best penetration airspeed glide, there are an infinite number of ways to transition into flight in ground effect. Fortunately, there are a number of practical considerations that limit the ways a transition could be made. First, a

second dive (manuever 3) must be made at a steeper dive angle than the best penetration airspeed dive in order to significantly change the glide range from a standard profile. Since gliders lack sophisticated intruments to allow complex dives, the only dive which could be done consistently is a constant pitch angle dive. A constant pitch angle dive equates to a constant flight path angle (γ) dive for low α ; therefore, the third manuever in the test profile is a constant γ dive. Second, a glider pilot will only have time to fly one dive besides the initial best penetration dive. This is because the dive (test manuever 3) must be initiated close to the ground and there simply isn't time to transition to another dive before ground impact would occur. Third, a glider pilot cannot fly a complex step down into ground effect. The lack of height references at very low altitudes makes complex step downs difficult, and even highly experienced glider pilots have difficulty judging a precise height AGL. Therefore, the best manuever in ground effect that a glider pilot can consistently fly is a constant height AGL deceleration, which is test manuever 5. Fourth, physics demand that some type of pushover connect test manuevers 1 and 3 and some type of pullup connect test manuevers 3 and 5. Good glider pilots can perform constant load factor pushovers and pullups consistently, but without any complex instrumentation they cannot perform any other types of

pushovers and pullups consistently. Thus, test maneuvers 2 and 4 were defined as a constant load factor pushover and pullup respectively. This accounts for all 5 test maneuvers shown in Figure 5.4.

Applying the reasoning of the previous paragraph to the standard profile, standard maneuver 2 must be a constant load factor pullout and standard maneuver 3 must be a level deceleration. Note that standard maneuver 3 is identical to the portion of test maneuver 5 where the airspeeds in both maneuvers are equal. This important result implies that a level deceleration in ground effect need not be tested below an airspeed slightly below the best penetration airspeed in order to determine the range difference between the test and standard profiles. This result is fortunate, because safety of flight considerations did not allow flight testing in ground effect at low airspeeds. Grob testing was terminated on both standard and test profiles at 50 KTAS; Blanik testing was also terminated at 50 KTAS with flaps up and 40 KTAS with flaps down.

Profile Familiarization Flights.

Eleven Grob sorties were flown to familiarize the test pilots with the test flight profile shown in Figure 5.4. Initially, tests were flown above 500 feet AGL and pointed out 2 valuable safety and operational considerations in the test maneuvers. An important safety consideration

discovered was that constant angle dives (test maneuver 3) of more than 10 degrees would be unsafe at low altitudes. Dives up to 25 degrees were safely flown at high altitudes, but dives were restricted to 10 degrees during all profile testing at low altitudes. The operational consideration discovered was that very gentle pushovers and pullups were best to achieve a 10 degree dive angle. The test pilots found that load factors of up to 0.9 and 1.05 were best to smoothly push over and pull out to precise flight conditions. More aggressive pushovers and pullouts caused significant overshoots of the desired dive angle and heights of transition. Limiting the load factors of the maneuvers makes sense aerodynamically also because more aggressive maneuvers generate greater control drag. Therefore, the constant angle dives were limited to 10 degrees, and the pushover and pullup load factors were limited to 0.9 and 1.05 respectively.

The last profile familiarization flights were flown closer to the ground. No problems were encountered, and the details of how to fly the profiles were ironed out. The profile sequence began with a best penetration airspeed glide toward the speed course shown in Figure 1.1. The pilot would use spoilers to adjust his flight path above 350 feet AGL in order to arrive at 350 feet AGL over the distance reference vehicle. The reference vehicle was set back from the speed course by a distance (X_{ref}) determined

from the glider simulation such that the glider would enter the speed course at the start of the level deceleration. The glider then began the pushover at a set altitude above ground level, established and maintained a constant angle dive until reaching a given airspeed, and then pulled out at a constant load factor to begin the level deceleration at a given altitude AGL.

The simulation provided 6 target parameters for each maneuver that completely defined the test profile, and these parameters were verified on several familiarization profiles. These 6 target parameters were: the distance for the reference vehicle (X_{ref}), the height to begin the pushover (h_{push}), the load factor of the pushover (n_{push}), the dive angle of the constant angle dive (θ_{dive}), the load factor of the pullout ($n_{pullout}$), and the height of the level deceleration (h_{decel}). Several other target parameters were generated to help the pilots fly the profiles, but only these 6 are needed to completely define the profile. These familiarization flights therefore proved that the test flight profiles were viable.

Flight Profile Development

After the flight profile familiarization flights, a series of 34 sorties were flown on 2 consecutive days to develop flight profiles to test the gliding range of the Grob without wind. The test profiles for these flights were

developed from optimization results using an early version of the glider simulation. These flights proved that a test profile flown under ideal conditions could extend Grob gliding range by up to 1179 feet over the standard flight profile currently used.

An early version of the glider simulation was used with the steepest gradient optimization algorithm to determine the profiles to be tested. The test profile parameters were designed to encompass variations of the predicted optimum profile for maximum glide range. The early glider simulation version was used because the rapid flight test schedule precluded data analysis from the level decelerations and therefore the simulation could not be updated with the deceleration results. The early simulation version used the Grob out of ground effect drag polar and the lifting line predictions of ground effect. This resulted in the simulation parasite drag coefficient being 11.6 percent less than actually seen in the level decelerations, and the simulation induced drag factor was likewise up to 16 percent low at altitudes below 10 feet. The steepest gradient algorithm used the early simulation to predict what the optimum profile for maximum gliding range without wind would be. The steepest gradient algorithm is described in Chapter IV and was run twice using a set of starting parameters clearly greater than a solution could be and using a set of starting parameters clearly less than the solution could be.

The 2 runs of the algorithm each converged in 5 iterations to within 5 percent of each other. This steepest gradient optimization of the early simulation therefore served its purpose by providing a first guess at the optimum flight profile for maximum range without wind.

The test matrix in Table 5.2 was built to encompass 32 variations of 4 pushover altitudes, 2 pushover load factors, 2 dive angles, and 2 level deceleration altitudes. Four practice profiles were also included at 2 higher level deceleration altitudes to give the aircrew practice on the first 2 runs of each day. The test matrix also planned for 2 standard profiles to establish the standard range against which to measure the test profiles. Unfortunately, 4 factors reduced the utility of the 34 profiles flown using this test matrix. First, radar tracking was available on only 19 of the 34 profile test sorties flown, reducing the number of useful profile tests to 19. Second, the Grob altimeter had about a 50 foot mechanical lag error; this resulted in all pushover altitudes being 50 feet too high. Third, the difficulty in eyeballing dive angles made all constant angle dives flown lie within 3 degrees of 10 degrees nose down. Fourth, all pushover load factors were flown within 0.02 of 0.95; even with a sensitive mechanical G-meter the test pilots could not achieve a variation in pushover load factor in addition to all of the other parameters they were required to achieve. These factors

TABLE 5.2

Flight Profile Development Test Matrix

Profile Number	H _{push} (feet)	n _{push} (G)	γ _{dive} (deg)	n _{pull} (G)	H _{decel} (feet)	Remarks
1	---	---	--	1.05	4	Std Profile
2	---	---	--	1.05	4	Std Profile
3	250	0.9	10	1.05	15	Practice
4	250	0.9	10	1.05	15	Practice
5	250	0.9	10	1.05	10	Practice
6	250	0.9	10	1.05	10	Practice
7	250	0.95	10	1.05	4	*
8	200	0.95	10	1.05	4	
9	175	0.95	10	1.05	4	
10	150	0.95	10	1.05	4	
11	250	0.9	10	1.05	4	
12	200	0.9	10	1.05	4	
13	175	0.9	10	1.05	4	
14	150	0.9	10	1.05	4	
15	250	0.95	10	1.05	6	
16	200	0.95	10	1.05	6	
17	175	0.95	10	1.05	6	
18	150	0.95	10	1.05	6	
19	250	0.9	5	1.05	6	
20	200	0.9	5	1.05	6	
21	175	0.9	5	1.05	6	
22	150	0.9	5	1.05	6	
23	250	0.95	5	1.05	4	
24	200	0.95	5	1.05	4	
25	175	0.95	5	1.05	4	
26	150	0.95	5	1.05	4	
27	250	0.9	5	1.05	4	
28	200	0.9	5	1.05	4	
29	175	0.9	5	1.05	4	
30	150	0.9	5	1.05	4	
31	250	0.95	5	1.05	6	
32	200	0.95	5	1.05	6	
33	175	0.95	5	1.05	6	
34	150	0.95	5	1.05	6	

* Originally Predicted Optimum Profile

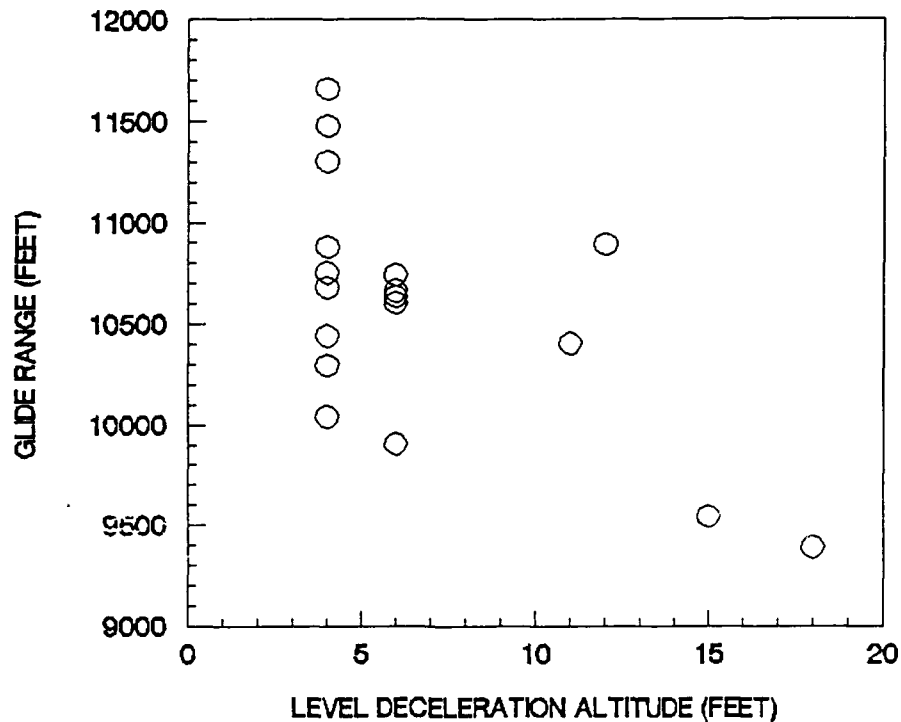


FIGURE 5.5: Glide Range Versus Level Deceleration Altitude

reduced the amount and variations of the test profiles, but the test results were sufficient to evaluate the glider simulation and identify trends within the profiles tested.

Table 5.3 shows the results of the optimum profile tests along with the ranges predicted by the early version of the glider simulation. The only significant profile variations achieved were variations in the level deceleration altitude and in the pushover altitude.

Figure 5.5 is a compilation of test results with pushover altitudes between 290 and 240 feet, and it has a general trend showing the importance of the level deceleration altitude in determining glide range. The trend

TABLE 5.3

Profile Development Test Results

LEVEL DECEL ALTITUDE (feet)	PUSHOVER ALTITUDE (feet)	RANGE FROM 350 FEET AGL		
		MEASURED (feet)	SIMULATION PREDICTION	
			ORIGINAL (feet)	REVISED (feet)
18	278	9385	9923	9757
15	310	9540	9736	9623
12	281	10892	10206	10007
11	273	10402	10373	10109
6	291	9901	10699	10061
6	240	10738	11136	10578
6	239	10632	11129	10565
6	205	10661	11326	10887
6	205	10600	11340	10887
4	318	10293	10796	9942
4	309	10039	10837	10066
4	279	10440	11147	10416
4	261	10878	11287	10697
4	259	10677	11316	10715
4	232	11475	11480	10963
4	224	10750	11560	11084
4	217	11656	11623	11378
4	216	11300	11571	11364
4	Standard Profile	10477	10966	10951

of lower level deceleration altitudes giving more range is skewed somewhat by the various pushover altitudes within each level deceleration set, but the overall trend is still

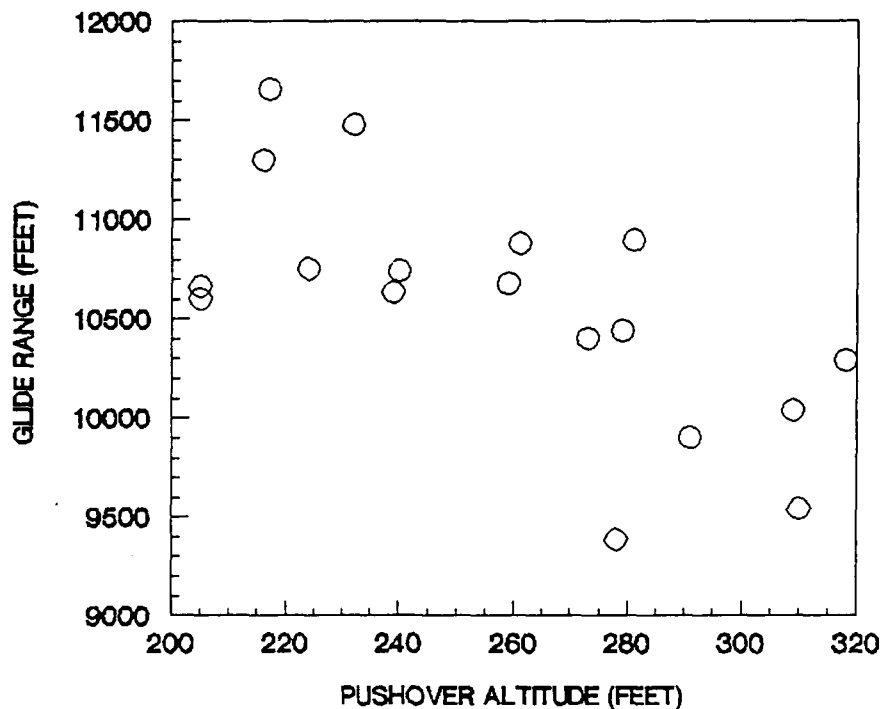


FIGURE 5.6: Glide Range Versus Pushover Altitude

apparent. The lowest possible level deceleration altitude is best because it provides the greatest reduction in induced drag from ground effect. Figure 5.6 graphs glide range versus pushover altitude. The pushover altitude also influences the glide range because it determines how fast the glider will be flying at the start of the level deceleration. Within each group of level deceleration altitudes, lower pushover altitudes gave better range down to the minimum altitude tested. These trends were confirmed by the revised glider simulation, and the revised simulation matched the flight test results within 400 feet of range for all but 1 point.

While the results of Table 5.3 show that a ground effect flight profile can increase range up to 1179 feet over a standard profile, the results are somewhat misleading. The standard profile shown in the table was flown at a penetration speed about 5 knots too slow and therefore did not give as much range as it should have. The comparisons between optimum flight profiles using ground effect and standard profiles are made in Chapter VI using the glider simulation and they show that the optimum flight profile using ground effect extends maximum range only slightly over a perfectly flown standard profile. The importance of these tests were that they showed that the revised glider simulation indeed matches the flight test data closely.

Flight Profile Verification

Having developed and verified methods of predicting ground effect, and having demonstrated a range gain with the Grob G-103 in ground effect, the next test phase was to validate these methods on a different glider. The Blanik was different from the Grob in 3 major ways as shown in Table 5.4: it had a lower aspect ratio, a high mounted wing, and a higher C_{D0} and k . The lower aspect ratio and higher C_{D0} and k gave the Blanik worse glide performance than the Grob. The high mounted wing prevented the Blanik from flying any lower than 7 feet AGL and reduced the

TABLE 5.4
Test Aircraft Comparison

CHARACTERISTIC	GROB	BLANIK	
		FLAPS UP	FLAPS DOWN
Wingspan (feet)	57.4	53.1	53.1
Wing Area (ft ²)	191.6	206.1	248
Aspect Ratio	17.1	13.7	11.4
Test Weight (lbs)	1279	1102	1102
C _{Do}	0.010675	0.012	0.019
K ₀	0.02296	0.046	0.0328

benefits of ground effect. The Blanik was more representative of a production glider because its drag characteristics had not been flight test verified for 5 years and could have changed significantly. The Blanik was tested in 2 configurations because the 2 configurations were very different in aspect ratio and were slightly different in wing area. Thus, the 2 configurations essentially represented 2 different gliders which gave our methods a good test of production gliders.

Fourteen data runs were flown in the Blanik sailplane: 7 with flaps-up and 7 with flaps-down. This time, the constant angle dives were standardized at 10 degrees and the pushover and pullup load factors were standardized to 0.9 and 1.05 Gs respectively. Unfortunately, this test like the Grob profile tests also suffered from lack of radar data in

TABLE 5.5

Profile Verification Test Matrix

CONFIGURATION	RUN NO.	LEVEL DECEL ALTITUDE (feet)	PUSHOVER ALTITUDE (feet)	REMARKS
Flaps Up	1	7	---	Standard Profile
	2	15	200	Practice Profile
	3	7	200	*
	4	7	175	
	5	7	150	
	6	7	125	
	7	7	100	
Flaps Down	8	7	---	Standard Profile
	9	15	200	Practice Profile
	10	7	200	*
	11	7	175	
	12	7	150	
	13	7	125	
	14	7	100	

* Originally Predicted Optimum Profile

that only 7 of the 14 runs were tracked. Once again, the mechanical lag error of the altimeter made all pushover altitudes about 50 feet higher than planned. Table 5.5 lists the test matrix as planned, and Table 5.6 lists the test results.

The test matrix in Table 5.5 and the original range predictions in Table 5.6 were developed using the steepest

TABLE 5.6
Profile Verification Test Results

CONFIG- URATION	LEVEL	PUSHOVER ALTITUDE (feet)	RANGE FROM 350 FEET AGL		
	DECEL		MEASURED (feet)	PREDICTED BY SIMULATION	
	ALTITUDE (feet)			ORIGINAL (feet)	REVISED (feet)
Flaps Up	7	197	7825	8902	8436
	7	172	7719	8888	8411
	7	164	8200	8970	8497
	7	Standard Profile	7825	8792	8673
Flaps Down	7	137	6926	7566	7209
	7	125	7027	7603	7278
	7	Standard Profile	7528	7543	7457

gradient optimization algorithm on a simulation of the Blanik with 5 year old flight test drag characteristics and uncorrected lifting line ground effect predictions. As with the Grob profile tests, the speed of the test schedule did not allow the simulation to be updated prior to flight test. The original predictions were up to 1100 feet too optimistic, but the revised predictions were much closer for the flaps down configuration. The revised predictions used the simulation with the lifting line ground effect theory revised at low altitude and a revised Blanik drag polar.

The Blanik C_{D0} was increased 11.6 percent based on the Grob level deceleration test results to account for the added control drag encountered in flying these high gain tests. The revised predictions matched flaps down flight test results very well (within 300 feet), but the flaps up results were 600 to 800 feet short of the revised predictions. These large differences indicate that the Blanik probably has a greater flaps up C_{D0} than the published Blanik data. This demonstrates a practical drawback to the optimum profile predictions because almost all production gliders have published drag polars that show more optimistic performance than they actually have. In view of these results, the optimum profile methods should not be used on a glider whose drag characteristics are not known within 5 percent.

VI. Flight Profile Optimization

Methods

After completion of the flight test program described in Chapter V, a revised glider simulation was optimized using the steepest gradient algorithm and Newton's method. This optimization yielded the optimum profiles to fly for maximum glide range with and without wind.

The glider simulation was revised after the level deceleration flight tests showed that ground effect did not effectively reduce induced drag as much as originally predicted by the lifting line theory. The ground effect model was modified to match the level deceleration test results at heights below 17.5 percent wingspan. Also, the level deceleration tests showed that the parasite drag of a glider increases by about 11.6 percent during the demanding task of flying a ground effect profile. The simulation was revised to increase the parasite drag coefficient during level decelerations by 11.6 percent accordingly. These 2 revisions made the simulation more accurate in flight profile tests of the Grob and the Blanik, and these revisions will now be used to predict optimum flight profiles for maximum range with and without wind.

The turbulent boundary layer wind model discussed in Chapter II was also used in the simulation. This wind model gives the reduction in wind velocity at a given altitude AGL

caused by ground effect.

Penetration Airspeed Computation.

The penetration airspeeds for each glider at each wind speed were computed using the quadratic spline interpolation method discussed in Chapter IV. This method gave a penetration airspeed within 0.25 knots of the actual penetration airspeed, which is more accurate than any glider pilot could fly. The penetration airspeed was used in the glider simulation in the first maneuver of the optimum flight profile, and it represents the best airspeed to fly in order to maximize glide range out of ground effect.

The derivation of the penetration airspeed may be visualized with a glider performance polar which shows the glider's vertical velocity versus true airspeed. The Grob performance polar out of ground effect is shown in Figure 6.1 as an example. To determine the penetration airspeed from the performance polar, the ratio of the groundspeed to the vertical velocity must be maximized. Since groundspeed is equal to the true airspeed minus the wind velocity, the ratio of groundspeed to vertical velocity is maximized by a tangent to the performance polar which intersects the wind velocity point on the horizontal axis. This penetration airspeed is equal to the airspeed for the maximum lift to drag ratio in no wind conditions and grows increasingly as wind velocity grows.

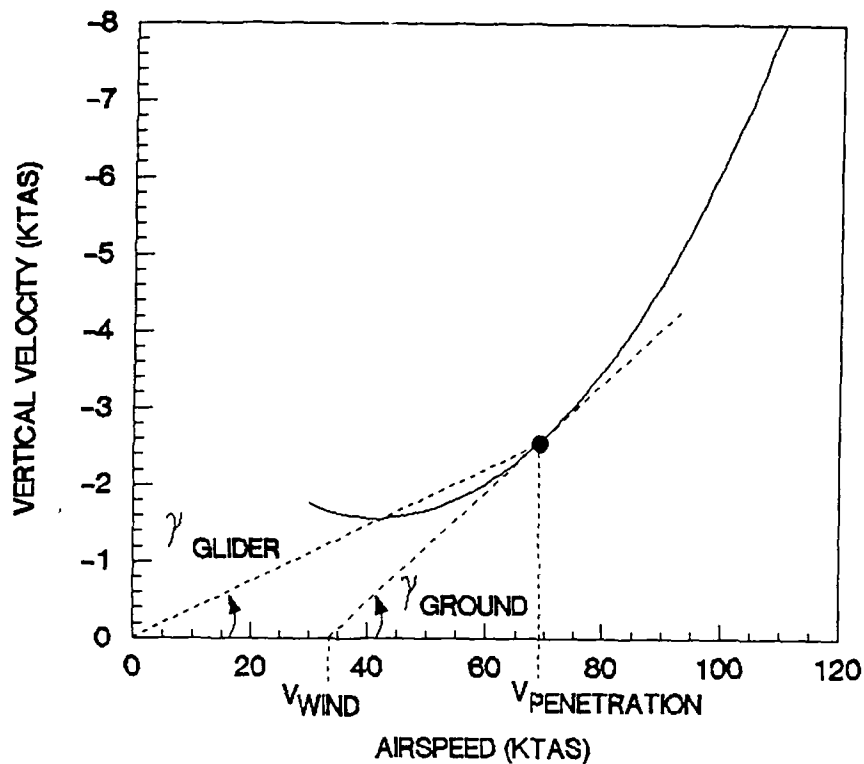


FIGURE 6.1: Grob Performance Polar

Using equations 3.4 and 3.8, the flight path angle γ_{glider} can be expressed as a function of the true airspeed V . Noting that the flight path angle γ_{glider} is constant in a penetration dive yields the result $n = \cos(\gamma_{\text{glider}})$ from equation 3.4. Substituting this result and the identity $\cos^2(\gamma_{\text{glider}}) = 1 - \sin^2(\gamma_{\text{glider}})$ into equation 3.8 and noting that the airspeed V and induced drag factor k_0 remain constant during a penetration airspeed dive out of ground effect yields:

$$0 = W \sin(\gamma_{\text{glider}}) - \frac{\rho V^2 S C_{D0}}{2} - \frac{2 W^2 k_0}{\rho V^2 S} + \frac{2 W^2 k_0}{\rho V^2 S} \sin^2(\gamma_{\text{glider}}) \quad (6.1)$$

Equation 6.1 can now be solved for $\sin(\gamma)$ by taking the positive root of the quadratic function as shown below:

$$\sin(\gamma_{\text{glider}}) = \frac{-W + \left\{ W^2 - 4 \left(\frac{2 W^2 k_0}{\rho V^2 S} \right) \left[-\frac{\rho V^2 S C_{D0}}{2} - \frac{2 W^2 k_0}{\rho V^2 S} \right] \right\}^{0.5}}{2 \left(\frac{2 W^2 k_0}{\rho V^2 S} \right)} \quad (6.2)$$

The ground approach angle γ_{ground} in Figure 6.1 represents the angle of descent of the glider with respect to earth fixed coordinates. A minimum γ_{ground} gives the highest ratio of horizontal groundspeed to vertical velocity. From the geometry of Figure 6.1, the following expression can be derived for $\tan(\gamma_{\text{ground}})$:

$$\tan(\gamma_{\text{ground}}) = \frac{V \tan(\gamma_{\text{glider}})}{V - V_{\text{wind}}} \quad (6.3)$$

Since γ_{glider} is a relatively small angle (typically less than 5 degrees for penetration glides in winds up to 50 KTAS), $\sin(\gamma_{\text{glider}})$ will be used to approximate

$\tan(\gamma_{\text{glider}})$. Solving for γ_{ground} and substituting the expression for $\sin(\gamma_{\text{glider}})$ in equation 6.3 yields:

$$\gamma_{\text{ground}} = \tan^{-1} \left\{ \frac{V \left\{ -W + \left\{ W^2 - 4 \left(\frac{2 W^2 k_0}{\rho V^2 S} \right) \left[- \frac{\rho V^2 S C_{D0}}{2} - \frac{2 W^2 k_0}{\rho V^2 S} \right] \right\}^{0.5} \right\}}{2 (V - V_{\text{wind}}) \left(\frac{2 W^2 k_0}{\rho V^2 S} \right)} \right\} \quad (6.4)$$

This expression for γ_{ground} in terms of V was solved numerically using the quadratic spline interpolation algorithm discussed in Chapter IV to give the best penetration airspeed to fly in a given wind. The angle γ_{ground} is equivalent to the function g in Equation 4.17 and the single independent variable V is equivalent to q . The algorithm always converged to a solution within 0.25 knots of the best possible solution in 8 to 10 iterations. This best penetration airspeed was then used as the starting maneuver for the optimum flight profile for maximum glide range.

Flight Profile Optimization.

Two parameters in the flight profile in Figure 5.4 were varied in order to determine the optimum profile for maximum range. The penetration dive angle at the start of the profile was naturally set by the penetration airspeed, and

the pushover and pullup load factors were set to 0.9 and 1.05 respectively because the test pilots in the optimum profile flight tests felt most comfortable with these load factors in low altitude maneuvering. The level deceleration altitude was set such that the lowest point on the glider was 1 foot AGL because this was the lowest that the test pilots could fly with special height references. This left the height of starting the pushover and the angle of the constant angle descent as the 2 remaining variables to be optimized, but even these 2 variables needed 2 safety constraints. The height of the pushover was constrained to be at least 100 feet AGL because beginning a dive below 100 feet AGL would be unsafe. The angle of the constant angle descent was limited to a maximum of 10 degrees nose down because steeper flight path angles would be unsafe.

Using the revised simulation with the wind model and the calculated penetration airspeed, the steepest gradient algorithm and Newton's method were used in combination to find the optimum profiles for maximum glide range with and without wind. The steepest gradient algorithm and Newton's method are described in detail in Chapter IV. Both methods were used to optimize the pushover height and constant angle dive of the flight profile shown in Figure 5.4. The glide range X was equivalent to the function g in these algorithms, and the variables of the pushover height and the dive angle were equivalent to the variables x and y . The

TABLE 6.1
Grob Optimum Profiles

HEAD- WIND	PENE- TRATION AIRSPEED	H _{push}	N _{push}	DIVE ANGLE	N _{pull}	H _{decel}	GLIDE RANGE GAIN OVER STD PROFILE
(KTAS)	(KTAS)	feet	(G)	(deg)	(G)	(feet)	(feet)
0	55.6	100	0.9	8.2	1.05	4	142
10	58.2	117	0.9	8.4	1.05	4	267
20	62.4	150	0.9	8.8	1.05	4	346
30	67.7	204	0.9	9.5	1.05	4	463
50	85.4	410	0.9	10.0	1.05	4	560

steepest gradient algorithm was used on this flight profile for 3 to 5 iterations and provided an approximate solution for use with Newton's method. Newton's method provided a very good solution such that the values of the variables were changing less than 1 percent on each iteration.

Results

Table 6.1 shows the optimum profiles for maximum range in the Grob. Several logical trends are apparent in these results. First of all, the penetration airspeeds increase as the headwind velocity increases. This is logical since a glider must fly faster to overcome a headwind. Secondly, the pushover altitudes of each optimum profile increase as wind velocity increases. This makes sense because the reduction in wind velocity at low altitudes makes

TABLE 6.2

Blanik Flaps Up Optimum Profiles

HEAD- WIND	PENE- TRATION AIRSPEED	H _{push}	N _{push}	DIVE ANGLE	N _{pull}	H _{decel}	GLIDE RANGE GAIN OVER STD PROFILE
(KTAS)	(KTAS)	feet	(G)	(deg)	(G)	(feet)	(feet)
0	57.3	137	0.9	8.2	1.05	7	266
10	60.3	160	0.9	8.4	1.05	7	307
20	64.4	188	0.9	8.8	1.05	7	317
30	69.9	215	0.9	9.5	1.05	7	324
50	86.8	480	0.9	10.0	1.05	7	337

transitioning into ground effect more advantageous at the higher wind velocities. Thirdly, the optimum profile uses the maximum dive angle available. In the low altitude profiles, there was insufficient time to reach the dive angle limit of 10 degrees, but the maximum angle possible at each pushover height was always reached. This again is logical, since a steep dive gives a quick transition into the ground effect reductions of wind and drag. Lastly, the ground effect profile range gain over a standard profile increases as wind velocity increases. This also makes sense due to the wind reduction caused by ground effect at low altitudes.

The optimum profiles for the Blanik with flaps up in Table 6.2 and with flaps down in Table 6.3 show the same trends as the Grob profiles did. The penetration airspeed, pushover start height, and range gain all increase with

TABLE 6.3

Blanik Flaps Down Optimum Profiles

HEAD- WIND	PENE- TRATION AIRSPEED	H _{push}	N _{push}	DIVE ANGLE	N _{pull}	H _{decel}	GLIDE RANGE GAIN OVER STD PROFILE
(KTAS)	(KTAS)	feet	(G)	(deg)	(G)	(feet)	(feet)
0	42.8	100	0.9	10.0	1.05	7	45
10	45.9	100	0.9	9.8	1.05	7	91
20	50.7	108	0.9	9.7	1.05	7	107
30	57.9	135	0.9	9.5	1.05	7	113
50	79.7	177	0.9	10.0	1.05	7	117

increasing wind velocity, and the dive angle optimized was the maximum available under the applied constraints.

The optimum profiles in Tables 6.1 to 6.3 also show the effects of the differences between the Grob and the Blanik. The 2 gliders are similar in wingspan, wing area, and gross weight as shown in Appendix A. The Blanik's high wing and pitch sensitivity cause it to fly 3 feet higher than the Grob, which reduces ground effect significantly. The Blanik with flaps up has a 12 percent higher profile drag coefficient than the Grob and twice its induced drag factor. The higher induced drag factor causes a greater range gain than the Grob at low wind speeds, but this range gain falls off due to the higher profile drag at the high speeds required to overcome higher winds. The Blanik with flaps down has a 78 percent higher parasite drag coefficient

than the Grob and a 43 percent higher induced drag factor. The higher parasite drag coefficient causes a lesser range gain than the Grob at all wind speeds. This comparison of the Blanik and the Grob shows that the range gain is maximum for a low winged high performance glider such as the Grob in headwinds over 20 knots. The Blanik with flaps up has slightly greater range gains in winds less than 20 knots.

Since the Grob has more range in headwinds and since most glider pilots who are interested in ground effect fly high performance gliders, the Grob was used for parametric trade studies to determine the effects of varying 7 key parameters. The density altitude, level deceleration height, penetration airspeed, wingspan, wing loading, parasite drag coefficient, and induced drag factor were varied separately to determine their effects on the range gained by using a ground effect profile versus a standard profile. These results show that the ground effect profile works better than a standard profile at high density altitudes, at low level deceleration heights, at penetration airspeeds less than optimum, and with gliders having long wingspans, high wing loadings, low parasite drag coefficients, and high induced drag factors.

Figure 6.2 shows the range gained with an optimum ground effect profile over a standard profile at density altitudes from sea level to 10,000 feet. Glide range in absolute terms varies considerably with density altitude,

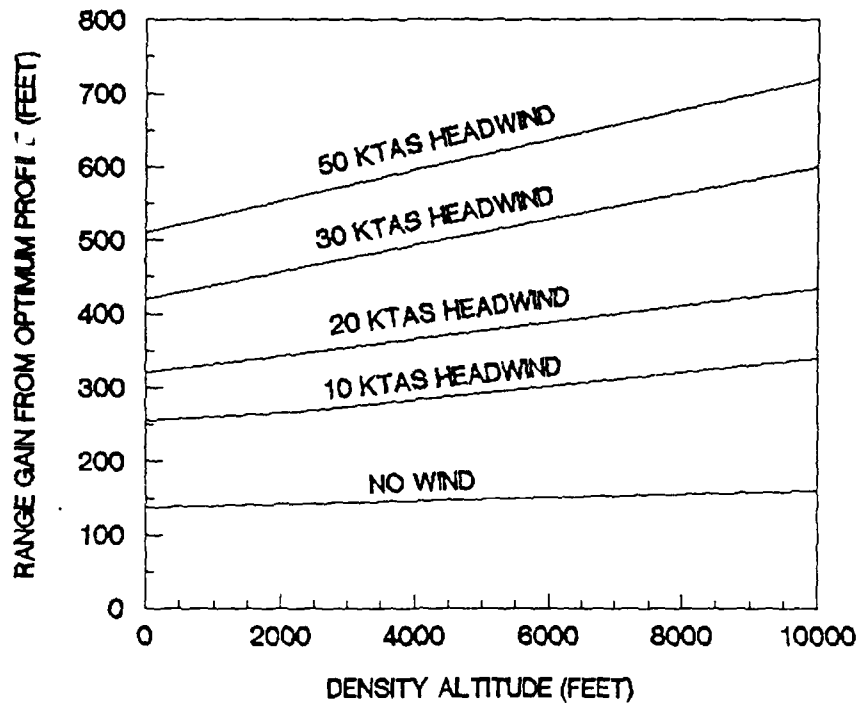


FIGURE 6.2: Range Gain Versus Density Altitude

but the gain in range from using a ground effect profile versus a standard profile has less variation because both profiles vary somewhat similarly with density altitude. The range gain variation between sea level and 10,000 feet is only 16.3 percent with no headwind because it varies directly with true airspeed. True airspeed is a function of the ratio of the square root of air densities as shown in equation 6.5 below.

$$V_2 = V_1 \left(\frac{\rho_1}{\rho_2} \right)^{0.5} \quad (6.5)$$

Once headwinds are present, the range gained using ground effect is greater than equation 6.5 would predict. This greater range gain is caused by the fact that a glider at high altitudes travels at a higher true airspeed and therefore has a higher groundspeed in a wind of given velocity. This does not mean that gliders typically would normally experience greater range gains at high altitudes because the winds at higher altitudes are typically greater than those at lower altitudes. It does mean that a glider would experience a greater range gain using a ground effect profile at a higher altitude at a given wind speed, however.

Figure 6.3 shows the range gained in no wind conditions by using an optimum ground effect profile at various level deceleration height to wingspan ratios. Range gain increases rapidly with decreasing height to wingspan ratios due solely to ground effect induced drag reduction. This reduction in induced drag causes a range loss at heights above 20 percent of the Grob's wingspan, which is a much lower cutoff than many glider pilots would think. Although this result applies specifically to the Grob, most medium to high performance gliders are sufficiently similar that they would not see any range gain at level deceleration heights above 20 percent wingspan in no wind conditions. An altitude of 20 percent wingspan equates to 11.5 feet AGL in most high performance aircraft, and the need to fly at such low altitudes in no wind conditions severely limits the

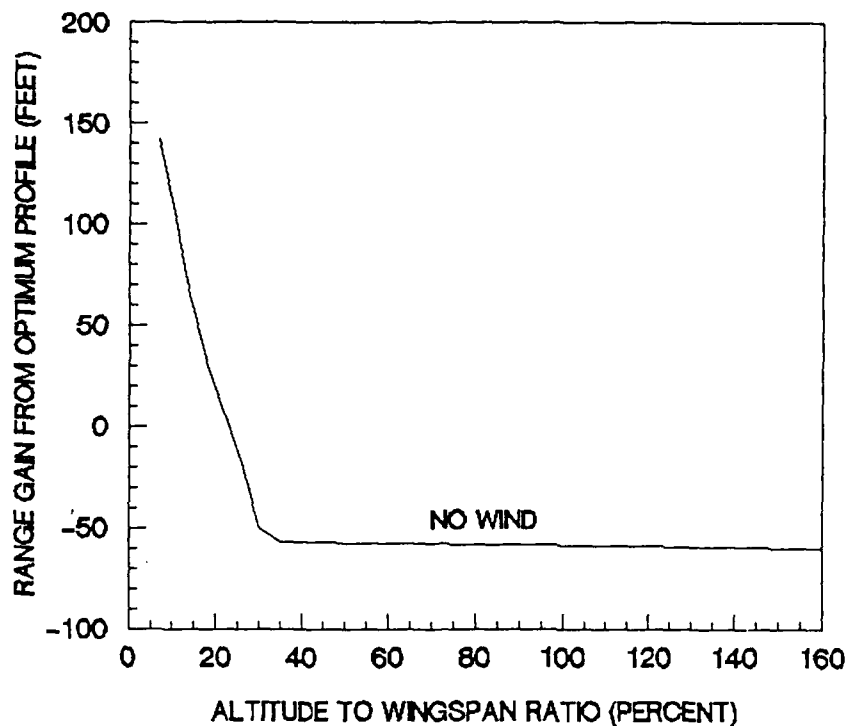


FIGURE 6.3: Range Gain Versus Altitude to Wingspan Ratio

usefulness of the ground effect optimum profile.

Figure 6.4 shows the range gained by using an optimum ground effect profile at various level deceleration altitudes AGL. The wind curves in Figure 6.4 are not a function of height to wingspan ratio since the wind reduction due to ground effect is a function of absolute altitude AGL only. Wind reduction due to ground effect can cause range gains at much higher altitudes than under no wind conditions. Up to 300 feet of range could be gained in 50 knot headwinds using a level deceleration altitude of 90 feet, which is sufficient to clear most obstacles existing

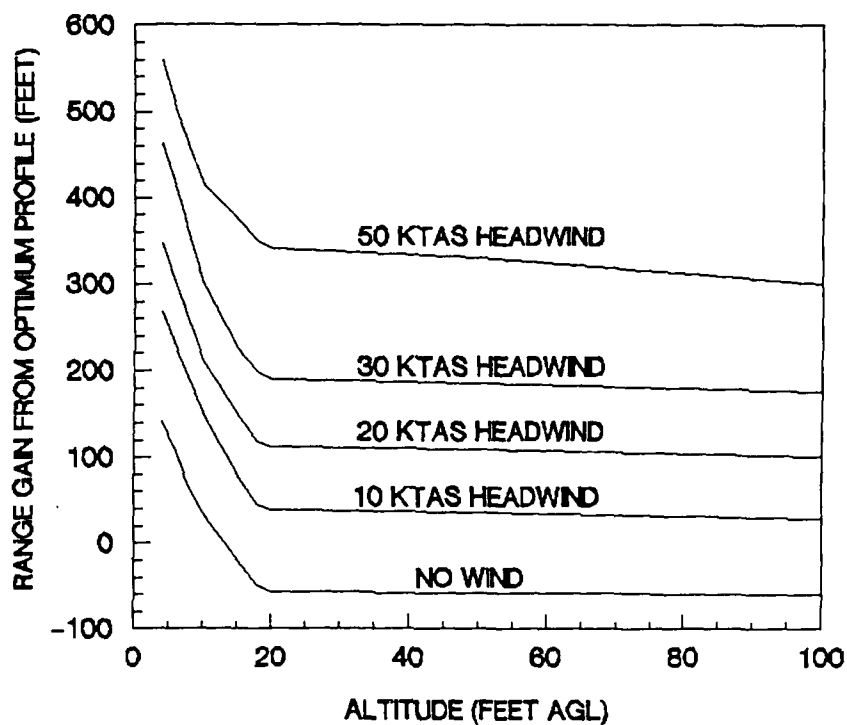


FIGURE 6.4: Range Gain Versus Level Deceleration Altitude

near glider airfields. High winds generally bring many other problems such as turbulence and updrafts or downdrafts, however. These problems make flying at even 90 feet AGL dangerous.

Glider pilots rarely have precise wind measurements when soaring, and most glider pilots do not have the McReady ring to compute their best penetration speed when they encounter a wind. Therefore, a glider pilot could easily misjudge his penetration airspeed by up to ± 10 knots. Flying the wrong penetration airspeed will change glide range as shown in Figure 6.5. Flying too low a penetration airspeed shortens range in the standard profile, resulting

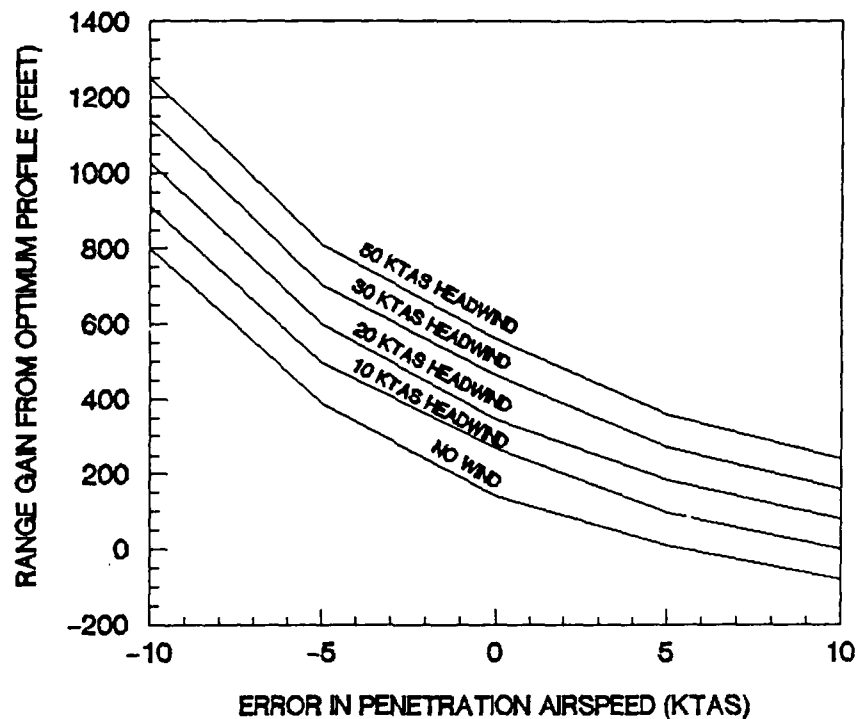


FIGURE 6.5: Range Gain Versus Error in Penetration Airspeed

in a greater range gain from flying an optimum ground effect profile. Flying too high a penetration airspeed makes the standard profile more like an optimum ground effect profile and therefore decreases range gained using the ground effect profile. Thus, if the penetration airspeed is not precisely known or the airspeed indicator is not accurately calibrated, a standard profile should be flown about 2 knots faster than the estimated penetration speed for each 10 knots of headwind. This faster airspeed will make the profile more like an optimum profile without having the dangerous characteristics of an optimum profile and will guard against the large range losses that occur at airspeeds

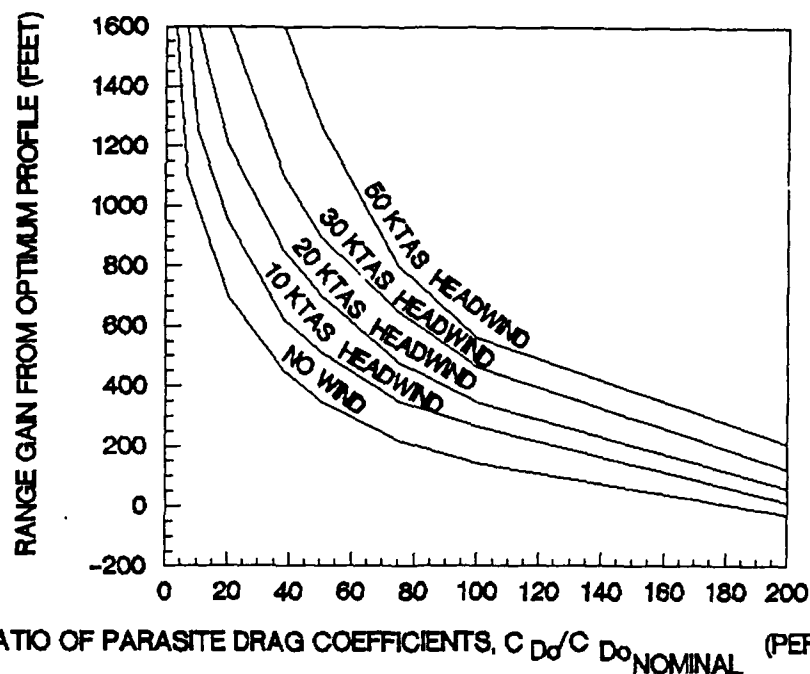


FIGURE 6.6: Range Gain Versus Variation in Parasite Drag Coefficient

below penetration airspeed.

Figure 6.6 shows how the aircraft parasite drag coefficient greatly affects the range gain possible using an optimum ground effect profile. Lower parasite drag coefficients cause greater range gains because the glider transitions into ground effect from a higher altitude and spends more time in ground effect. Some high performance gliders have lower parasite drag coefficients than the Grob, but most do not have significantly lower coefficients and would not see significantly greater range gains than a Grob.

Figure 6.7 shows the variation of range gain due to an optimum profile versus aircraft wing loading. A high wing loading causes maximum range gain with the ground effect

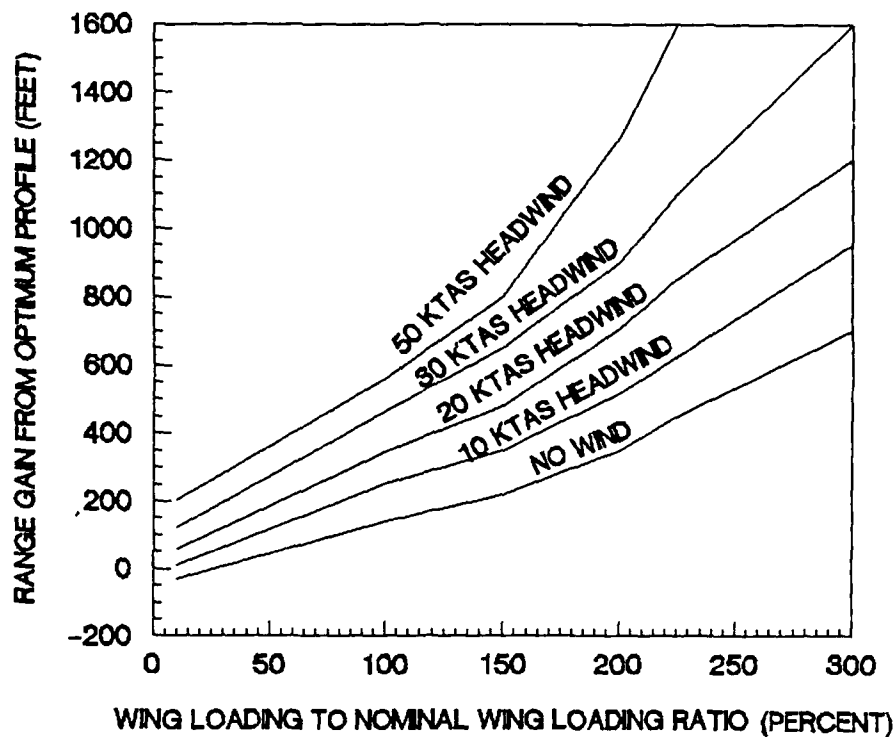


FIGURE 6.7: Range Gain Versus Wing Loading Variation

profile because the glider operates at higher angles of attack where induced drag is prevalent. This effect does not help most high performance gliders because they are designed to be as light as possible and thus do not have wing loadings much higher than the Grob.

High induced drag factors can cause a slightly greater range gain for the ground effect profile as Figure 6.8 shows. This is because a greater induced drag means that more induced drag is reduced by ground effect. Conversely, a large decrease in range gain would result from decreasing k_0 . The parasite drag coefficient could easily be increased, but decreasing k_0 beyond the low value shown by

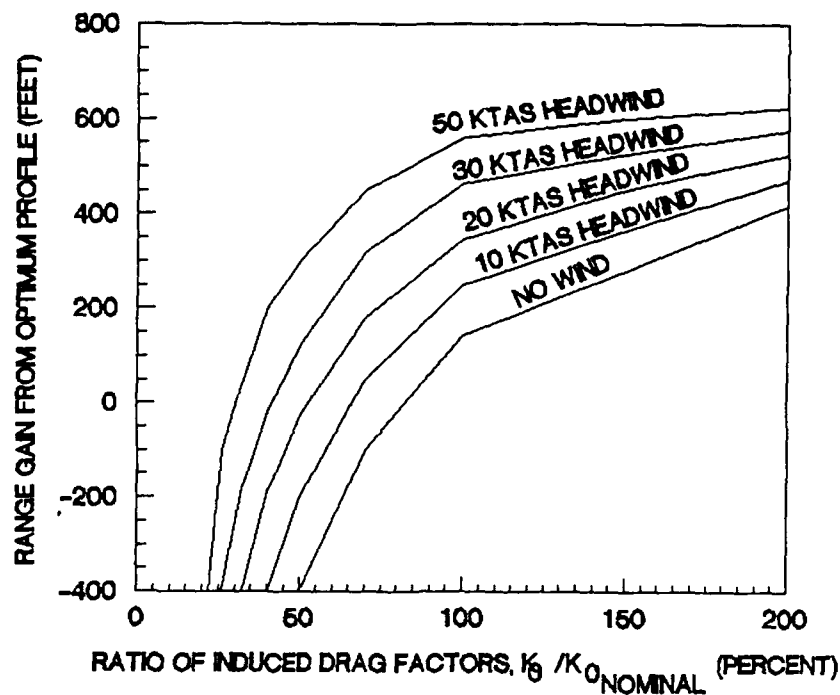


FIGURE 6.8: Range Gain Versus Variation in Induced Drag Factor

the Grob would be difficult. As shown in Chapter II, k_0 depends inversely on aspect ratio and wing efficiency. The Grob has a high aspect ratio of 17.1; few gliders have significantly greater aspect ratios. The wing efficiency is determined primarily by the lift distribution across the wingspan; an elliptical lift distribution is optimum. The lift distribution of the Grob could not be significantly improved without reducing the aspect ratio. Thus, most other glider configurations have higher induced drag factors and would see a greater range gain from ground effect profiles.

Practical Applications

Despite having predicted and proven that an optimum ground effect profile can increase glide range over the standard maximum range profile currently flown, the applications of ground effect are limited by several safety and operational concerns. These concerns limit ground effect application to a very few special cases.

The small increases in glide range possible using an optimum ground effect profile are not practical and are not worth the risks in normal circumstances. Most glider airfields have some obstacles and lack good low altitude height references, which makes flying low enough for reducing induced drag almost impossible. If strong headwinds are present, then moderate to strong air turbulence will likely be present, and flying smoothly enough to avoid generating extra control drag would be almost impossible. This extra control drag would nullify any gains resulting from the reduction of wind velocity due to ground effect. Also, most gliders have not been flight tested recently to confirm their drag characteristics; from the Blanik flight tests we have learned that knowing the aircraft drag characteristics very precisely is crucial to developing the optimum ground effect profile. Finally, most glider pilots have not practiced these maneuvers and could not fly a ground effect profile smoothly enough to allow it to increase glide range. Furthermore, the risks inherent in

flying the optimum ground effect profile in production gliders without special instruments are not worth the marginal range gains that are theoretically possible. All of these factors make the ground effect profiles impractical and unsafe for general soaring use.

Some limited uses of ground effect might be possible for aircraft other than gliders. The wind reduction and induced drag reduction caused by ground effect could be used in emergencies by powered aircraft on overwater flights to extend range or maintain flight under low power. There have been unconfirmed stories of a B-17 maintaining flight on one engine using ground effect on a flight to Hawaii during the early part of World War II. Also, man powered aircraft use ground effect to reduce drag and headwinds. Some slow flying light aircraft and powered airships could use the reduction in headwind velocity caused by ground effect at altitudes up to 275 feet AGL to increase groundspeed, but flights at these low altitudes should be done very cautiously. These special cases are the only safe and practical uses for ground effect on conventional aircraft.

VII. Conclusions and Recommendations

Conclusions

This research has met its 2 main goals of evaluating ground effect theory and developing the optimum flight profiles for maximum gliding range. All 8 specific objectives listed in Chapter I were also accomplished. Although this research has shown that ground effect is not practical or safe to use in extending glide range, the project did provide useful insight and valuable flight test data on ground effect.

A glider simulation was developed and revised which accurately predicted glider range performance. The 3 degree of freedom simulation had a visual display capability and could simulate flight in wind or windless conditions. The simulation was limited to gentle maneuvers, but these maneuvers were adequate to evaluate the ground effect profiles due to the safety constraints on the maneuvers. The simulation matched Grob flight test results within 400 feet for 18 of 19 flight profiles flown and was the basis for the optimizations used to determine the optimum flight profile for maximum glide range.

The airspeed instrument errors and the drag polar of the Grob G-103 were determined out of ground effect to allow accurate flight testing and simulation of the Grob. The airspeed instrument errors were determined through ground

tests and trailing cone static source flight tests out of ground effect. These instrument errors were verified in ground effect using radar gun velocity data and allowed the test pilots to fly very accurate airspeeds during flight tests. The Grob drag polar was estimated using aircraft design methods and then measured using timed constant airspeed descents out of ground effect. The design methods gave parasite drag coefficients within 19 percent of the flight test data, but the induced drag factors were up to 43 percent more than the flight test data. The induced drag factor discrepancy shows a breakdown in the low aspect ratio design methods when used on high aspect ratio gliders. The flight test drag parameters were used in the simulation and allowed the evaluation of how the Grob drag polar changed in ground effect flight tests.

The amount of drag reduction in ground effect was flight test determined at 8 altitudes ranging from 100 to 4 feet AGL. Radar position and velocity data were taken at 1 second intervals on 47 level decelerations flown in the Grob. The steepest gradient and Gauss-Newton optimization algorithms were used with the glider simulation to determine the drag reduction due to ground effect inherent in these data. The results of these tests showed that the lifting line derived predictions of induced drag reduction due to ground effect matched flight test results down to 10 feet AGL but were up to 16 percent too optimistic below 10 feet.

These test results indicate that there may be additional viscous drag at low altitudes which the lifting line theory does not account for. In any case, glider performance at altitudes below 10 feet AGL is less than the lifting line theory would predict. A revised prediction of ground effect applicable to glider performance was developed and is shown in Figure 5.3.

Flight test profiles were developed and flown in the Grob to test glide range with and without ground effect. Radar data were taken on 19 profiles flown in the Grob to evaluate the glide range of variations of pushover altitudes and dive angles. These profiles showed that the lowest pushover altitudes and the steepest dive angles safely possible gave the best glide range in ground effect. A range gain of 1179 feet was demonstrated over the standard non-ground effect profile that glider pilots currently fly, but this range gain was mostly due to the fact that the standard profile was flown about 5 knots slower than the best penetration speed.

Radar data were taken on 7 flight profiles flown in the Blanik to determine if the simulation and ground effect predictions of the Grob could be applied to production gliders. The Blanik was tested with flaps retracted and extended to give 2 very different glider configurations and in effect test 2 different gliders. The revised simulation matched the results of the flaps down tests within 300 feet

but missed the flaps up test results by up to 850 feet. The flaps up results show that accurate ground effect predictions cannot be made for most production gliders because the drag characteristics of most production gliders are not accurately known.

A numerical method of determining the best penetration speed for a glider with known drag characteristics in a headwind was developed, and an important observation about the penetration airspeed was made from the glider simulation. The quadratic spline interpolation algorithm was used to approximate the penetration airspeed within 0.25 knots. This method would be useful to any glider pilot who wanted to know his best penetration airspeeds for a variety of winds prior to flight. Once these speeds are known, however, the glider simulation showed that flying an airspeed slightly faster than the penetration airspeed is far better than flying a slower than penetration airspeed. Therefore, if there is any uncertainty in the penetration airspeed or if the glider airspeed indicator has not been calibrated a glider pilot should fly about 2 knots above the estimated penetration airspeed for every 10 knots of wind.

Optimum flight profiles were developed for the Grob and Blanik gliders to provide maximum gliding range with and without headwinds. The steepest gradient algorithm and Newton's method were used in combination to provide very precise profile parameters to fly in order to achieve

maximum range. Unfortunately, the range gains from these profiles were not more than 600 feet over the range provided by standard profiles currently flown. Safety and operational considerations outweigh these marginal range gains, and these optimum flight profiles are not recommended for general soaring use.

Trade studies of 7 key parameters were made to determine their effects on the range which could be gained using an optimum flight profile versus a standard flight profile. The following factors in order of importance cause an optimum flight profile to gain range over a standard profile:

1. Low level deceleration altitude.
2. Long wingspan.
3. Low parasite drag coefficient.
4. High wing loading.
5. High induced drag factor.
6. Flying at a less than optimum penetration speed.
7. High density altitude.

Although this research established that using ground effect to extend glide range is not practical or worth the risks involved, the research did contribute to the knowledge of ground effect. The most important contributions of this research are the revised predictions of ground effect and the methods of predicting glide range in ground effect. This information will benefit soaring pilots and special

flight projects which are considering using ground effect to improve aircraft performance.

Recommendations

1. Glider pilots should NOT attempt to use ground effect to extend glide range as the small range gains given by optimum ground effect profiles are not worth the risks involved.

2. Future research considering the use of ground effect to improve light aircraft performance should focus on the reduction of wind velocity caused by ground effect. At 275 feet AGL, ground effect eliminates up to 10 percent of the wind velocity normally present at 900 feet AGL. This reduction in wind velocity can greatly improve the cruise performance of powered light aircraft at low altitudes. Future ground effect research may want to further validate the turbulent boundary layer atmospheric model and investigate the fact that wind directions change at low altitudes due to ground effect.

3. Future research interested in vehicles designed to operate in ground effect at very low altitudes should investigate the additional viscous drag due to lift which is not predicted by the inviscid lifting line theory. This research showed that up to 16 percent more induced drag was

present at low altitudes that the lifting line theory predicted; this additional drag could be very significant to a vehicle designed to operate using ground effect at low altitudes.

Appendix A
Glider Descriptions

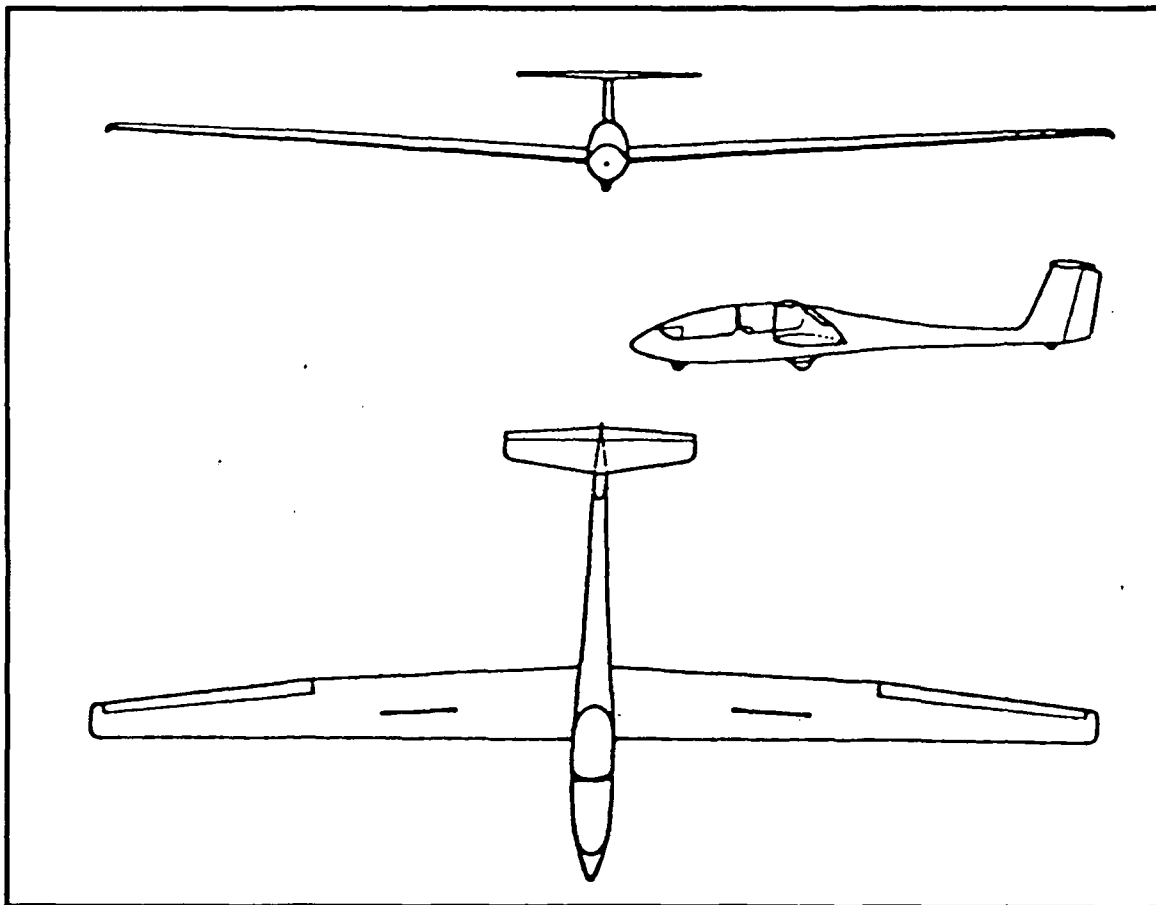


FIGURE A1: Grob G-103 Twin II

Manufacturer: Grob-Werke GmbH & Co. KG
Unternehmensbereich Burkhart Grob Flugzeugbau
8939 Mattsies, West Germany
(08268)411

Serial Number: 3793

Registration: N3950A

Grob G-103 Flight Manual Data

Wingspan	57 feet 5 inches
Length	26 feet 10 inches
Height	5 feet 1 inch
Wing Area	191.6 feet ²
Aspect Ratio	17.1
Empty Weight	838 pounds
Max Gross Weight	1,279 pounds
Max Payload	441 pounds
Max Wing Loading	6.67 pounds/foot ²
Center of Gravity Limit	24.7% to 43.6% \bar{c}
Min Load Front Seat	154.3 pounds

Max Loads:

Front Seat	242.5 pounds
Back Seat	242.5 pounds
Baggage Compartment	22.0 pounds

Max Speeds:

Rough Air (V_M)	92 Knots Calibrated Airspeed (KCAS)
Calm Air (V_{NE})	125 KCAS
Aero Tow	92 KCAS

Max Load Factors

Airspeed < V_M	+5.3 G
Airspeed < V_{NE}	+4.0 G

Min Load Factors

Airspeed < V_M	-2.65 G
Airspeed < V_{NE}	-1.5 G

1 G Stall Speeds at Max Gross Weight

Airbrakes Retracted	40 KCAS
Airbrakes Extended	46 KCAS

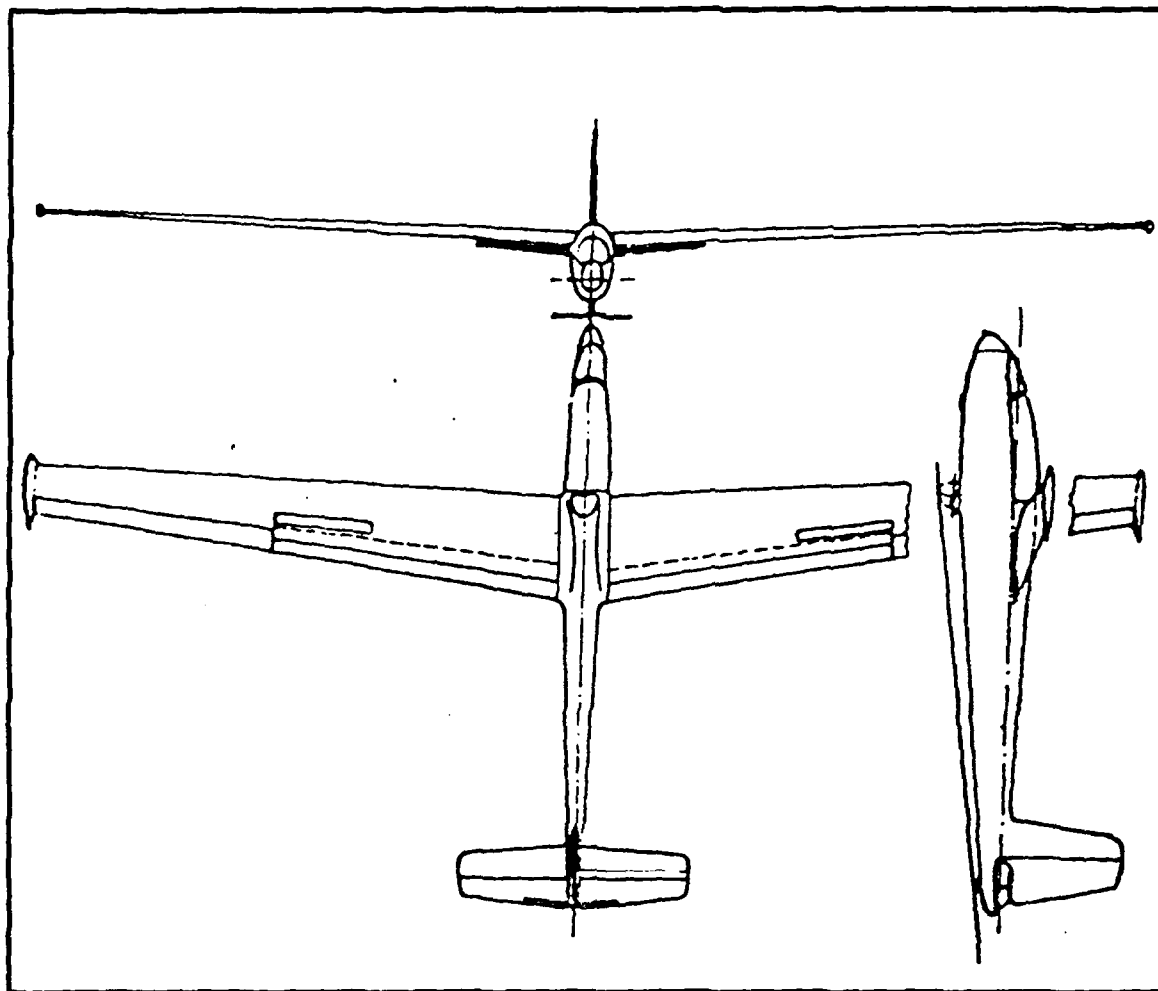


FIGURE A.2: Let L-13 Blanik

Manufacturer: Czechoslovakia Aeronautical Works
Letnany, Czechoslovakia

Serial Number: 027007

Registration: N70AS

Let L-13 Blanik Flight Manual Data

Wingspan	53 feet 1.75 inches
Length	27 feet 6.7 inches
Wing Area	206.13 feet ²
Aspect Ratio	13.7
Empty Weight	666 pounds
Max Gross Weight	1,102 pounds
Max Payload	436 pounds
Max Wing Loading	5.35 pounds/foot ²
Center of Gravity Limit	23% to 38% \bar{c}
Min Load Front Seat	150 pounds

Max Speeds:

Rough Air (V_M)	78 KCAS
Calm Air (V_{NE})	130 KCAS
Aero Tow	70 KCAS
Flaps Down	60 KCAS

Max Symmetric Load Factors

Weight < 880 pounds	+6.0 G
Weight < 1100 pounds	+5.0 G

Max Asymmetric Load Factors

Weight < 880 pounds	+5.0 G
Weight < 1100 pounds	+4.0 G

Min Load Factors

Weight < 880 pounds	-3.0 G
Weight < 1100 pounds	-2.0 G

1 G Stall Speeds at Max Gross Weight

Flaps Retracted	33 KCAS
Flaps at 30 Degrees	30 KCAS

Bibliography

1. Abbott, Ira C. and Von Doenhoeff, Albert E. Theory of Wing Sections. Dover Publications, New York, NY, 1959.
2. Burden, Richard L. and Faires, J. Douglas. Numerical Analysis. PWS Publishers, Boston, MA, 1985.
3. Class 88A, USAF Test Pilot School. USAFTPS-TR-88A-TM2: HAVE EFFECT Glider Ground Effect Investigation. USAF Test Pilot School, Edwards AFB, CA, December 1988.
4. Drela, Dr. Mark. MLE Tow Test Data Reduction. Handwritten Test Notes. Massachusetts Institute of Technology, October 1986.
5. Eppler, Richard. "Some New Airfoils." Science and Technology of Low Speed and Motorless Vehicles. NASA, Mar 29-30, 1979.
6. Hoerner, Dr. Sighard. Fluid-Dynamic Lift. Hoerner Fluid Dynamics, Brick Town, NJ, June 1975.
7. McRuer, Duane; Ashkenas, Irving; and Graham, Dunstan. Aircraft Dynamics and Automatic Control. Princetown University Press, Princetown, NJ, 1973.
8. Nicolai, Leland M. Fundamentals of Aircraft Design. Domicone Printing Services, Fairborn, OH, 1975.
9. Panofsky, Hans A. and Dalton, John A. Atmospheric Turbulence: Models and Methods for Engineering Applications. Pensylvania State University, PA, Undated.
10. Performance Phase Textbook. USAF Test Pilot School, Edwards AFB, CA, April 1986.
11. Quinn, Dr. Math 652 Course Handout. Air Force Institute of Technology, Wright Patterson AFB, OH, 1987.
12. Taylor, John W. R. Jane's All The World's Aircraft 1973-1974. Franklin Watts, New York, NY, 1973.
13. Taylor, John W. R. Jane's All The World's Aircraft 1979-1980. Franklin Watts, New York, NY, 1980.
14. TSPI Data Cover Sheet. Ripley Test Engineering Facility, Edwards AFB, CA, October 1988.
15. Wismer, David A. and Chattergy, R. Introduction to Nonlinear Optimization. Elsevier Science Publishing Company, New York, NY, 1978.

Vita

Captain Nathan H. Jones was born on 2 September 1961 in Memphis, Tennessee. He graduated from high school in Columbus, Georgia, in 1979 and entered the United States Air Force Academy. After graduating with distinction in 1983, he received a regular commission in the US Air Force and was assigned to the Air Force Armament Laboratory at Eglin AFB, Florida. He was reassigned to the Office for Aircraft Compatibility, 3246th Test Wing, Eglin AFB, in 1984 and served there until 1986. He then attended Squadron Officer School at Maxwell AFB, Alabama, and entered the Air Force Institute of Technology School of Engineering in August, 1986, under the joint AFIT-Test Pilot School program.

Permanent Address: 9767 Huntsman Path
Pensacola, Florida 32514

UNCLASSIFIED

SECURITY CLASSIFICATION OF THIS PAGE

REPORT DOCUMENTATION PAGE

1a. REPORT SECURITY CLASSIFICATION UNCLASSIFIED			1b. RESTRICTIVE MARKINGS	
2a. SECURITY CLASSIFICATION AUTHORITY			3. DISTRIBUTION/AVAILABILITY OF REPORT Approved for public release; distribution unlimited	
2b. DECLASSIFICATION/DOWNGRADING SCHEDULE				
4. PERFORMING ORGANIZATION REPORT NUMBER(S) AFIT/GAE/ENY/89J-2			5. MONITORING ORGANIZATION REPORT NUMBER(S)	
6a. NAME OF PERFORMING ORGANIZATION School of Engineering		6b. OFFICE SYMBOL (If applicable) AFIT/ENY		7a. NAME OF MONITORING ORGANIZATION
6c. ADDRESS (City, State and ZIP Code) Air Force Institute of Technology Wright-Patterson AFB, Ohio 45433			7b. ADDRESS (City, State and ZIP Code)	
8a. NAME OF FUNDING/SPONSORING ORGANIZATION		8b. OFFICE SYMBOL (If applicable)		9. PROCUREMENT INSTRUMENT IDENTIFICATION NUMBER
8c. ADDRESS (City, State and ZIP Code)			10. SOURCE OF FUNDING NOS.	
			PROGRAM ELEMENT NO.	PROJECT NO.
			TASK NO.	WORK UNIT NO.
11. TITLE (Include Security Classification) GLIDER GROUND EFFECT INVESTIGATION/UNCLASS.				
12. PERSONAL AUTHOR(S) Nathan H. Jones, B.S., Capt, USAF				
13a. TYPE OF REPORT MS Thesis		13b. TIME COVERED FROM _____ TO _____		14. DATE OF REPORT (Yr., Mo., Day) 1989 May
15. PAGE COUNT 132				
16. SUPPLEMENTARY NOTATION				
17. COSATI CODES			18. SUBJECT TERMS (Continue on reverse if necessary and identify by block number)	
FIELD	GROUP	SUB GR		
01	01		Aerodynamics, Drag, Flight Testing	
19. ABSTRACT (Continue on reverse if necessary and identify by block number) This research used glider flight tests and optimized glider simulations to evaluate the aerodynamics of ground effect and to determine the optimum flight profile for maximum gliding range in gliders. A series of 122 sorties were flown in the Grob G-103 Twin II and the Let L-13 Blanik gliders on a specially designed very low altitude speed course at the Air Force Flight Test Center, Edwards AFB, California from 21 September to 25 October 1988. Radar tracking data were used to determine the glider position and velocity, and a 3 degree of freedom glider performance simulation was used to determine the glider parasite and induced drag coefficients in ground effect. Lifting line derived predictions of ground effect induced drag reduction developed by Dr. Sighard Hoerner were found to be accurate at altitudes				
20. DISTRIBUTION AVAILABILITY OF ABSTRACT UNCLASSIFIED/UNLIMITED <input checked="" type="checkbox"/> SAME AS RPT. <input type="checkbox"/> DTIC USERS <input type="checkbox"/>			21. ABSTRACT SECURITY CLASSIFICATION UNCLASSIFIED	
22a. NAME OF RESPONSIBLE INDIVIDUAL Major Daniel Gleason, USAF			22b. TELEPHONE NUMBER (Include Area Code) 805-227-4369	22c. OFFICE SYMBOL USAFTPS/TENR

Continuation of Block 19:

above 20 percent wingspan but were up to 16 percent too optimistic at low altitudes. A revised prediction of ground effect induced drag reduction was developed based on the flight test data, and this revised prediction was used along with a turbulent boundary layer wind model in two optimization algorithms to develop the optimum flight profiles for maximum range gliding flight. Although flight tests of these profiles in near perfect test conditions showed that glide range gains of up to 1179 feet were possible over penetration airspeed glides, these profiles involve dangerous low altitude maneuvers and are not predicted to give significant range gains over penetration airspeed glides in winds up to 500 knots. Therefore, the results of this research are a revised prediction of ground effect at low altitude and the confirmation that penetration airspeed glides provide maximum glide range under normal circumstances.